



TITLE:

Long - Term Density Trend in the Mesosphere and Lower Thermosphere From Occultations of the Crab Nebula With X - Ray Astronomy Satellites

AUTHOR(S):

Katsuda, Satoru; Enoto, Teruaki; Lommen, Andrea N.; Mori, Koji; Motizuki, Yuko; Nakajima, Motoki; Ruhl, Nathaniel C.; ... Tashiro, Makoto S.; Terada, Yukikatsu; Wood, Kent S.

CITATION:

Katsuda, Satoru ...[et al]. Long - Term Density Trend in the Mesosphere and Lower Thermosphere From Occultations of the Crab Nebula With X - Ray Astronomy Satellites. *Journal of Geophysical Research: Space Physics* 2023, 128(2): e2022JA030797.

ISSUE DATE:

2023-02

URL:

<http://hdl.handle.net/2433/279487>

RIGHT:

© 2023. The Authors.; This is an open access article under the terms of the Creative Commons Attribution-NonCommercial-NoDerivs License, which permits use and distribution in any medium, provided the original work is properly cited, the use is non-commercial and no modifications or adaptations are made.

JGR Space Physics

RESEARCH ARTICLE

10.1029/2022JA030797

Key Points:

- Time series of combined O and N densities are measured in the MLT, based on atmospheric occultations of the Crab Nebula using X-ray astronomy satellites
- The density is decreasing everywhere, with a local minimum of -12% /decade near 105 km
- The local minimum in density trends may be due to strong cooling by water vapor and ozone, as was first predicted by Akmaev et al. (2006, <https://doi.org/10.1016/j.jastp.2006.03.008>)

Correspondence to:

S. Katsuda,
katsuda@mail.saitama-u.ac.jp

Citation:

Katsuda, S., Enoto, T., Lommen, A. N., Mori, K., Motizuki, Y., Nakajima, M., et al. (2023). Long-term density trend in the mesosphere and lower thermosphere from occultations of the Crab Nebula with X-ray Astronomy Satellites. *Journal of Geophysical Research: Space Physics*, 128, e2022JA030797. <https://doi.org/10.1029/2022JA030797>

Received 29 JUN 2022
Accepted 24 JAN 2023







Author Contributions:

Conceptualization: Satoru Katsuda, Koji Mori, Yuko Motizuki, Makoto S. Tashiro, Kent S. Wood
Formal analysis: Satoru Katsuda, Teruaki Enoto, Motoki Nakajima, Nathaniel C. Ruhl
Funding acquisition: Satoru Katsuda, Makoto S. Tashiro
Investigation: Satoru Katsuda
Methodology: Satoru Katsuda
Project Administration: Satoru Katsuda
Software: Satoru Katsuda, Andrea N. Lommen, Nathaniel C. Ruhl
Supervision: Yukikatsu Terada

© 2023. The Authors.

This is an open access article under the terms of the [Creative Commons Attribution-NonCommercial-NoDerivs License](https://creativecommons.org/licenses/by/4.0/), which permits use and distribution in any medium, provided the original work is properly cited, the use is non-commercial and no modifications or adaptations are made.

Long-Term Density Trend in the Mesosphere and Lower Thermosphere From Occultations of the Crab Nebula With X-Ray Astronomy Satellites

Satoru Katsuda¹ , Teruaki Enoto^{2,3} , Andrea N. Lommen⁴, Koji Mori^{5,6}, Yuko Motizuki⁷ , Motoki Nakajima⁸, Nathaniel C. Ruhl⁴ , Kosuke Sato¹, Gunter Stober⁹, Makoto S. Tashiro^{1,6} , Yukikatsu Terada^{1,6} , and Kent S. Wood¹⁰

¹Graduate School of Science and Engineering, Saitama University, Saitama, Japan, ²Department of Physics, Graduate School of Science, Kyoto University, Kitashirakawa Oiwake-cho, Kyoto, Japan, ³RIKEN Cluster for Pioneering Research, Wako, Japan, ⁴Haverford College, Haverford, PA, USA, ⁵Department of Applied Physics and Electronic Engineering, University of Miyazaki, Miyazaki, Japan, ⁶Institute of Space and Astronautical Science (ISAS), Japan Aerospace Exploration Agency (JAXA), Sagami-hara, Japan, ⁷RIKEN Nishina Center, Wako, Japan, ⁸School of Dentistry at Matsudo, Nihon University, Chiba, Japan, ⁹Institute of Applied Physics & Oeschger Center for Climate Change Research, Microwave Physics, University of Bern, Bern, Switzerland, ¹⁰Retired P. O. Box. 127, Nathrop, CO, USA

Abstract We present long-term density trends of the Earth's upper atmosphere at altitudes between 71 and 116 km, based on atmospheric occultations of the Crab Nebula observed with X-ray astronomy satellites, ASCA, RXTE, Suzaku, NuSTAR, and Hitomi. The combination of the five satellites provides a time period of 28 years from 1994 to 2022. To suppress seasonal and latitudinal variations, we concentrate on the data taken in autumn ($49 < \text{doy} < 111$) and spring ($235 < \text{doy} < 297$) in the northern hemisphere with latitudes of 0° – 40° . With this constraint, local times are automatically limited either around noon or midnight. We obtain four sets (two seasons \times two local times) of density trends at each altitude layer. We take into account variations due to a linear trend and the 11-year solar cycle using linear regression techniques. Because we do not see significant differences among the four trends, we combine them to provide a single vertical profile of trend slopes. We find a negative density trend of roughly -5% /decade at every altitude. This is in reasonable agreement with inferences from settling rate of the upper atmosphere. In the 100–110-km altitude, we found an exceptionally high density decline of about -12% /decade. This peak may be the first observational evidence for strong cooling due to water vapor and ozone near 110 km, which was first identified in a numerical simulation by Akmaev et al. (2006, <https://doi.org/10.1016/j.jastp.2006.03.008>). Further observations and numerical simulations with suitable input parameters are needed to establish this feature.

Plain Language Summary Numerical simulations have shown that, while an increase of greenhouse gases such as CO₂ in the atmosphere causes heating of the troposphere (near surface), it causes cooling of the middle and upper atmosphere, which is the so-called “greenhouse cooling.” The greenhouse cooling should result in atmospheric contraction and consequently a temporal density decrease at a fixed height. However, observational evidence for the density decrease has been scarce in the mesosphere and lower thermosphere (MLT: 80–110 km), owing to difficulty in measuring the density in this region. Here, we present the first direct measurements of long-term variations for combined N and O atom number density in the MLT, based on atmospheric occultations of the Crab Nebula observed with X-ray astronomy satellites. The combination of five X-ray astronomy satellites, ASCA, RXTE, Suzaku, NuSTAR, and Hitomi, allows us to explore density trends for a long period from 1994 to 2022. We take into account variations due to a temporal linear trend and the 11-year solar cycle, using linear regression techniques. As a result, we find a negative density trend of roughly -5% /decade at every altitude, with a local minimum of -12% /decade near 105 km. This is in reasonable agreement with the state-of-the-art numerical simulations.

1. Introduction

Understanding the changes of the middle and upper atmosphere is important to our life, as was illustrated by the discovery of the stratospheric ozone depletion. The importance is increasing, as we utilize the space environment for many purposes such as telecommunications, navigation, space tourism, and scientific projects to explore the universe. There are several known drivers of middle and upper atmosphere climate change, including the increase



Validation: Satoru Katsuda, Nathaniel C. Ruhl
Visualization: Satoru Katsuda
Writing – original draft: Satoru Katsuda
Writing – review & editing: Satoru Katsuda, Teruaki Enoto, Andrea N. Lommen, Koji Mori, Yuko Motizuki, Motoki Nakajima, Nathaniel C. Ruhl, Kosuke Sato, Gunter Stober, Makoto S. Tashiro, Yukikatsu Terada, Kent S. Wood

in greenhouse gas (mainly, water vapor and carbon dioxide) concentrations (e.g., Akmaev et al., 2006), changes in ozone concentration (e.g., Bremer & Peters, 2008), long-term solar and geomagnetic activity variations (e.g., Beig, 2011; Perrone & Mikhailov, 2019), and shifts in Earth's main magnetic field (e.g., Cnossen et al., 2016). Of these, the dominant cause of long-term trends in the upper atmosphere in recent decades is thought to be the increase of greenhouse gases (e.g., Akmaev et al., 2006; Cnossen, 2020; Qian et al., 2013).

The roles of greenhouse gases in the atmosphere are (a) heating the atmosphere in the troposphere (near surface) and (b) cooling the middle atmosphere above ~20-km altitude, which was first shown by computer simulations by Manabe and Wetherald (1967). Roble and Dickinson (1989) performed pioneering numerical simulations focusing on the middle and upper atmosphere above 60 km, followed by many researchers in both numerical simulations and observations (see, e.g., Danilov & Konstantinova, 2020; Laštovička, 2017, for recent reviews). Greenhouse gases, particularly CO₂, cool the middle atmosphere, because the density in the middle atmosphere is so low that CO₂ molecules (and all the other greenhouse gases) are optically thin to outgoing infrared radiation. In this condition, thermal energy transferred by collisions with ambient gas to the excited states of CO₂ is lost to space via its infrared radiation (e.g., Goessling & Bathiany, 2016, for a deeper understanding of CO₂-induced cooling). It is the enhancement of greenhouse cooling, via increases in CO₂ and other greenhouse gases, that changes the thermal balance and induces the long-term trends. The combination of lower atmosphere heating and middle atmosphere cooling is demonstrated on Venus, whose atmospheric composition is dominated by CO₂. The “greenhouse cooling” in the middle atmosphere results in contraction of the middle atmosphere, leading to a downward displacement of constant pressure surfaces (e.g., Akmaev et al., 2006). Combined with the exponential density decrease with increasing altitude, a density at a fixed height decreases with time. The fact that stronger long-term trends have been predicted and confirmed in the middle atmosphere rather than the troposphere makes studies of the mesosphere and lower thermosphere (MLT) important in predicting climate changes.

The density trends in the thermosphere (~300-km altitude and above) have been extensively studied from satellites' orbit drag. Various researchers came to the conclusion that the density trend at ~400 km is negative at about a few %/decade with a possible solar-cycle dependence, ranging from -5%/decade for solar minimum conditions to -2%/decade for maximum conditions (e.g., Emmert et al., 2008, and references therein). The latest results as well as reviews of previous work can be found in Emmert (2015). The observational trend is in reasonable agreement with the state-of-the-art numerical simulations (e.g., Cnossen, 2020; Solomon et al., 2015).

The trend study in the MLT (80–110-km altitude) is also of great importance, especially because volume mixing ratio (VMR) of CO₂ rapidly falls off in this region due to molecular diffusive separation (as CO₂ is heavier than the mean molecular weight of the air) and photolysis. According to Whole Atmosphere Community Climate Model (WACCM) simulations (e.g., López-Puertas et al., 2017), the CO₂ VMR decreases from 380 ppmv below 80 km to 120 ppmv at 110-km altitude. Observationally, the CO₂ VMR is relatively difficult to be quantified in this region (Laštovička & Jelínek, 2019, for a review of observations). The most recent measurements are consistent with the model at the bottom of the MLT, but depart from the model with increasing altitude in the sense that the model underestimates the data (e.g., Garcia et al., 2016), posing challenges to our current understanding of dynamics, energetics, and photolysis in the MLT region. The long-term trend of the air density in the MLT region can be a new indicator of the trend of the CO₂ VMR trend.

Despite its importance, measurements of density trends in the MLT region are still scarce due to difficulty in situ observations. Snap-shot measurements were performed from solar/stellar occultations (e.g., Determan et al., 2007; Norton & Warnock, 1968) as well as in situ measurements based on the falling sphere technique (e.g., Strelnikov et al., 2013, and references therein). Although these data provided precious opportunities to verify density models, they are not sufficient to explore long-term trends. There is only one indirect measurement of the long-term density trends in the MLT. This is based on meteor radar-echo observations which measure meteor peak flux altitudes and convert them to neutral air densities. The neutral density trend inferred by this method was $-5.8 \pm 1.1\%$ /decade at 91-km altitude (Stober et al., 2014). Because this is obtained at a single altitude, our knowledge of the long-term trend in the MLT region is obviously poor.

Here, we present the first direct measurements of long-term neutral density variations in the MLT (altitudes between 71 and 116 km), utilizing atmospheric occultations of the Crab Nebula observed with X-ray astronomy satellites. The X-ray occultation method allows us to measure atomic number densities integrated along the line of sight, i.e., the column densities. Because X-rays are directly absorbed by inner K-shell and L-shell electrons, X-rays see only atoms (within molecules). Thus, the X-ray occultation method cannot distinguish between

atoms and molecules, but we can obtain their total number density without complexity involved with chemical, ionization, and excitation processes. This is different from other methods of density measurements such as orbital drag which measures mass density, meteor radar which also effectively measures mass density when converting height to density, optical, and infrared remote-sensing techniques like TIMED/SABER (Russell et al., 1999) which typically infer the atmospheric pressure and temperature, which are easily convertible via the ideal gas law to the number density. More specifically, the X-ray occultation method allows us to derive column densities of combined N and O atoms, i.e., $N_{A,N+O} = 2 \times N_{M,N_2} + 2 \times N_{M,O_2} + N_{A,O}$, where subscripts A and M represent the atomic number density and molecular number density, respectively (other minor species such as NO, N, and OH do not contribute significantly to X-ray extinction). We cannot distinguish between N and O, because the energy dependence of photon cross-sections of N and O are similar with each other in the energy range of 1–100 keV.

A pioneering work on X-ray occultation sounding of the upper atmosphere was performed by Determan et al. (2007) who analyzed Earth's atmospheric occultations of the Crab Nebula obtained with the RXTE satellite. Historically, this paper was produced as a by-product of X-ray satellite navigation experiments; if the navigational state vector for the satellite is known with precision, then the horizon crossings can be used to extract diagnostic information about the state of the atmosphere. The history of the dual usage of X-ray horizon crossing transitions is summarized in Wood et al. (2020). Recently, Katsuda et al. (2021), hereafter Paper I, and Yu et al. (2022a, 2022b) applied the same technique to derive atmospheric vertical density profiles, using Japanese and Chinese X-ray astronomy satellites, respectively. In this paper, we analyze atmospheric occultation data of the Crab Nebula acquired with X-ray astronomy satellites, ASCA, RXTE, Suzaku, NuSTAR, and Hitomi to reveal long-term trend of the neutral density in the MLT region. The data were obtained between 1994 and 2022, providing a time span of 28 years. This is longer than two solar cycles, enabling us to remove/suppress the possible influence of the 11-year solar cycle. This paper is organized as follows. In Section 2, we describe observations analyzed in this paper. In Section 3, we describe data analysis and results. In Section 4, we interpret the analysis results. Finally, we give conclusions of this paper in Section 5.

2. Observations and Data Reduction

We analyze X-ray data during Earth occultations of the Crab Nebula, which is a remnant of a supernova explosion that occurred in 1054 AD, to obtain vertical density profiles of the MLT region. The essential requirements for the celestial source used for this technique are (a) that the source be either constant or not varying significantly during the time required for the atmospheric occultation (a minute or so) and (b) that it should be a point source or sufficiently point-like that the angular extent does not matter. It is known that the Crab Nebula is not a perfect standard candle (Wilson-Hodge et al., 2011). However, its degree of variability is not so rapid as to change the shapes of individual occultations, or affect the analysis. It is also well established that the Crab Nebula also has an angular extent of about an arcminute in X-rays around 1 keV and then decreases in angular extent with increasing X-ray energy. Given that the distance between the satellite and the tangent point is roughly 2,000 km, this angular extent corresponds to a tangent altitude extent of ~ 0.6 km the tangent point is where the line of sight is closest to the Earth and the tangent altitude is the height from the Earth at the tangent point. This is comparable with the error due to the satellite position uncertainty from two-line element (TLE: Data are accessible by sending special requests at <http://celestrak.com/NORAD/archives/request.php>) + Simplified General Perturbations Satellite Orbit Model 4 (SGP4), as we will quantify later in this section. One could worry from these rough estimates that the angular size of the Crab Nebula, which is slightly asymmetric, should be in the error analysis, because it might be of the same order as the satellite position error. However, while there is potential for the total angular extent to be a problem, the flux is concentrated toward the center of the Nebula and the pulsar contributes as a point source near the centroid of the Nebular emission (e.g., Figures 11–15 in Madsen et al. (2015)). Thus, it is reasonable to consider the Crab Nebula as effectively a point source.

Basic information about the X-ray occultation technique can be found in Paper I. Because most (if not all) X-ray astronomy satellites so far have used the Crab Nebula to perform their calibrations, there are numerous data sets for this standard candle on orbits. Here, we make use of them to reveal long-term trends of the air density. Specifically, we use data acquired with the X-ray astronomy satellites/instruments, ASCA/GIS (Ohashi et al., 1996; Tanaka et al., 1994), RXTE/PCA (Jahoda et al., 1996), Suzaku/XIS + PIN (Koyama et al., 2007; Mitsuda et al., 2007; Takahashi et al., 2007), NuSTAR/FPM (Harrison et al., 2013), and Hitomi/HXI (Nakazawa

Table 1
Capabilities of X-Ray Instruments Used in This Work

Parameter	ASCA/GIS	RXTE/PCA	Suzaku/XIS	Suzaku/PIN	NuSTAR/FPM	Hitomi/HXI
Field of view	24' in radius	1° FWHM	18' × 18'	34' × 34'	10' × 10'	9' × 9'
Spatial resolution ^a	3'	—	2'	—	1'	1'.7
Energy resolution ^b	13 at 6 keV	5 at 6 keV	46 at 6 keV	7 at 20 keV	45 at 20 keV	14 at 14 keV
Time resolution ^c	1 μs	0.24 ms/4 s	0.1 s	0.1 ms	61 μs	26 μs

^aThe angular resolution is given by half power diameter. RXTE/PCA and Suzaku/PIN are nonimaging instruments. ^bThe energy resolution is given by $E/\Delta E$. ^cThe RXTE/PCA time resolutions of 0.24 ms and 4 s are for ObsIDs 70018 and 92018, respectively.

et al., 2018; Takahashi et al., 2018). Capabilities of individual instruments are summarized in Table 1. The effective areas are plotted in Figure 1.

To remove possible seasonal biases, we concentrate on spring (± 30 days around the spring equinox) and autumn (± 30 days around the autumnal equinox), and analyze the two seasons separately. In fact, ASCA, Suzaku, and Hitomi observed the Crab Nebula only in these two seasons, whereas RXTE and NuSTAR observed it during the whole year. Given that the five X-ray satellites used in this paper are in the low-Earth orbits with low inclination angles, and that the declination angle of the Crab Nebula is $+22^\circ$ above the celestial equator, the majority of the data are obtained in the northern hemisphere. To eliminate/suppress possible latitudinal dependences of atmospheric density, we analyze data obtained only in the northern hemisphere. Consequently, all the data are acquired in a latitude range between 0° and 40° in the northern hemisphere. Because this latitude range is large, it would be ideal to divide the data even more finely by latitude. However, the limited number of data makes such an analysis difficult. Alternatively, we could reduce the latitude-dependent density variations by analyzing deviations from an appropriate model such as NRLMSIS 2.0. Although such a fine tuning will not be considered in the present work, it will be worthwhile in the future analysis.

In Table A1, we summarize basic information about all the data analyzed in this paper. The individual setting (or rising) occultations in the same observation sequences are combined together to improve the photon statistics. This merging process is reasonable, because these data are taken at the similar telescope tangent points (latitude and longitude) and local times with each other. The merged occultations are labeled with the same group number as shown in the last column of the table. We note that the photon statistics in the RXTE data are so rich that they need not be combined. From this table and Figure 2, which illustrates local time versus day of year for all the occultation scans analyzed, we can see that local times are approximately either midnight or noon for all of our data sets. Therefore, by analyzing the noon and midnight data separately, density variations caused by tidal waves with periods of 24 hr plus harmonics are removed naturally.

In Paper I, we did not use the satellite positions provided by the Suzaku and Hitomi housekeeping files, but rather recalculated their positions by using the TLEs to improve accuracies of their positions and consequently tangent altitudes. In the meantime, we realized that the original positions provided by JAXA, which we received after publishing Paper I, are actually more accurate than the TLE data and are used in this paper. Suzaku's position accuracy is not available, but is a few hundred meters, given that it is determined by radio ranging. This is an order of magnitude better than that for the TLE data, which will be evaluated later in this section. Because Hitomi carries a GPS (global pointing system) receiver, its position accuracy is < 1 m. The accuracy in the position of the RXTE satellite is $< \sim 450$ m with 99% confidence (Jahoda et al., 2006). Such accurate positions are recorded every 60 s. Unfortunately, this time resolution is insufficient for our analysis. Therefore, we interpolate the satellite positions by using a cubic spline interpolation method. The accuracy of the interpolated position becomes worse than the original precision, but is less than a few 100 m, which is sufficient for the following analysis.

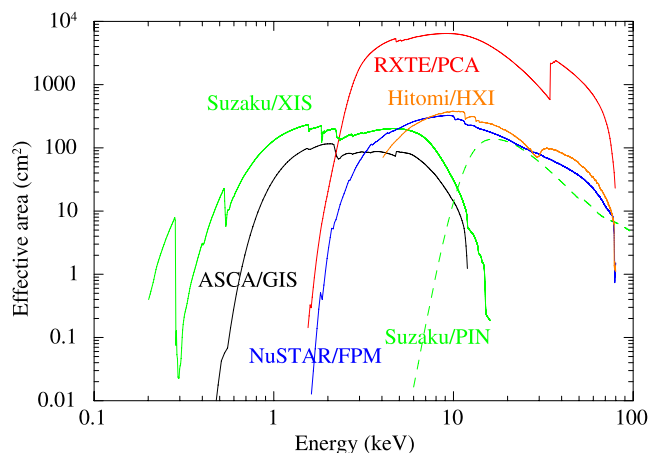


Figure 1. Comparison of the effective areas for the six instruments analyzed in this paper.

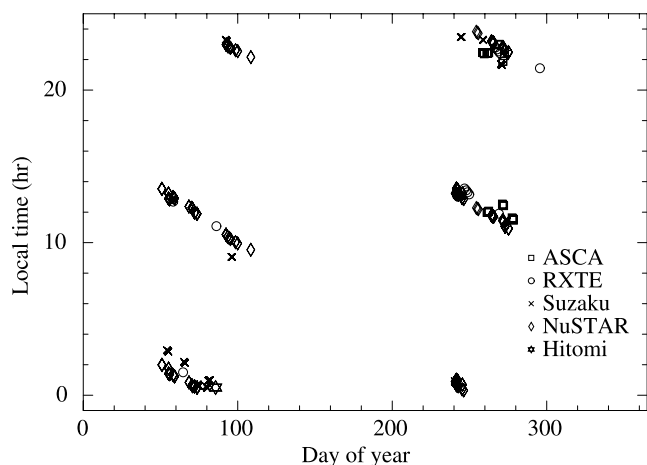


Figure 2. Local time at an altitude of 100 km for each occultation against the day of year.

As for ASCA and NuSTAR, no accurate satellite positions (with reasonable time intervals for ASCA) are available. Therefore, we calculate their positions based on TLE sets with SGP4, using the skyfield software written in python (available at <https://rhodesmill.org/skyfield/>). The uncertainty on the TLE-based satellite positions is estimated for the RXTE satellite by comparing the TLE-based positions and high-precision orbit data provided by the RXTE team. For this comparison, we do not perform the cubic interpolation but use original data with a cadence of 60 s to keep the original high precision. To increase the number of samples, we collect all occultation data of the Crab Nebula without constraints of the season and the latitude. As a result, we obtained a total of 140 occultations, most of which are not listed in Table A1. For each occultation, we calculate position differences between TLE and high-precision orbits for about 10 data points (~10 min) including the atmospheric occultation, and calculate their averages. The difference is calculated in altitude, latitude, and longitude directions, separately.

Figure 3 shows a cumulative fraction of the position differences in three directions, from which we derive the position uncertainties on the TLE as shown in Table 2. The fact that errors in the longitudinal direction are much larger than those in the other directions is reasonable, because TLEs tend to have larger errors in the in-track direction (Wang et al., 2009), which is close to the longitudinal direction for the RXTE with inclination angle of only 23°. In fact, the orbit errors associated with TLE + SGP4 measured for the CHAMP satellite (Xu & Xiong, 2018) are close to our measurement for the RXTE satellite. Thus, the errors in Table 2 seem typical for TLE-based positions for low-Earth-orbit satellites. In the next section, we will evaluate the impact of the spacecraft's position error to the measurement error on the air density.

3. Analysis and Results

We plot in Figure 4 example occultation light curves taken with each of the six instruments used in this paper. The gradual increase/decrease of the X-ray intensity along with the tangent altitude clearly shows the effect of atmospheric absorption. Also, the characteristic rising/setting altitudes significantly vary from instrument to instrument. This is due to the different energy coverage of each instrument, as shown in Figure 1 showing the effective area comparison for the six instruments. The higher the energy coverage of the instrument, the deeper the characteristic altitude. The altitude range to be analyzed for our spectral analysis is within dotted vertical lines in each panel, which is slightly different from instrument to instrument.

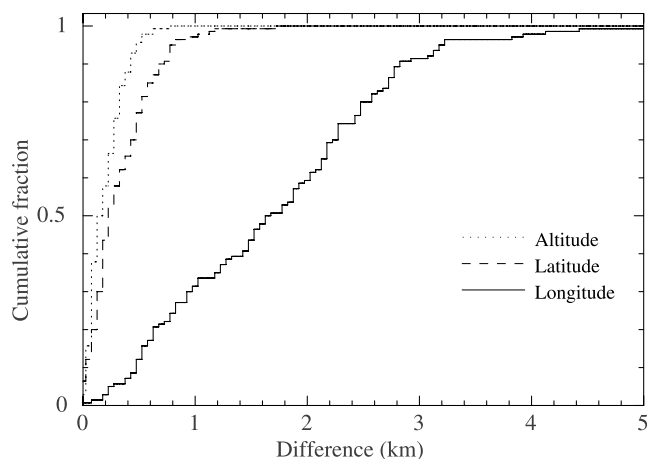


Figure 3. Cumulative fraction of the two-line element (TLE) errors in three directions. The TLE errors are defined as the difference between the RXTE position given in the orbit file (<~450 m at 99% confidence level) and that estimated from the TLE.

In principle, we can derive the atmospheric density profile by analyzing the light curves by using the Beer's law method (Aikin et al., 1993). This method is particularly useful for cases in which emission/absorption lines are analyzed, because one can know the accurate photoelectric cross-section at the photon energy of interest. On the other hand, the X-ray spectrum from the Crab Nebula is a power-law continuum. In this case, it is not very easy to specify a photon energy for a light curve, leading to a substantial uncertainty on the cross-section. Therefore, we analyze the X-ray spectrum to derive vertical atmospheric density profiles. In this case, it is technically easy to take account of the energy-dependent absorption cross-section, by utilizing the XSPEC package (Arnaud, 1996) which is a standard spectral analysis software in the X-ray astronomy.

We measure vertical density profiles for each of data group defined in Table A1. The procedure is almost the same as we did in Paper I, but some modifications and improvements are applied as described in the next few paragraphs. Briefly, we extract X-ray spectra from an altitude layer between 71 and 116 km, with a resolution of 6 km for each occultation data group. Every 6-km layer is overlapped with adjacent layers by half to derive smooth density profiles. An exception is Suzaku/XIS for which the data were

Table 2
TLE Errors for the RXTE Satellite

Direction	1-sigma C.L. (km)	90% C.L. (km)
Longitude	±1.1	±1.4
Latitude	±0.22	±0.35
Altitude	±0.13	±0.21

obtained in a special model, i.e., an exposure time of 0.1 s with a cadence of 8 s. As Suzaku moves in orbit, the tangent altitude increases/decreases at a speed of ~ 2 km/s near a tangent altitude of 100 km. Thus, the altitude bin of the XIS data corresponds to ~ 0.2 km and the data are taken every ~ 16 -km altitude. This is too sparse for binning by 6 km. On the other hand, thanks to the high throughput of the combined three coaligned XISs, the exposure time of 0.1 s (or 0.2-km altitude resolution) is sufficient for us to perform spectral analysis. Thus, we analyze the XIS spectra without binning.

When observing very bright sources like the Crab Nebula, ASCA/GIS, Suzaku/PIN, and NuSTAR/FPM have substantial deadtimes, i.e., the periods when the system is unable to record another event after the recording of each of new events. For example, the ASCA/GIS has a typical deadtime of about 8 ms per event (Makishima et al., 1996). Thus, in our spectral analysis, we perform deadtime corrections for ASCA/GIS, Suzaku/PIN, and NuSTAR/FPM, for which deadtime fractions for the Crab Nebula exceed 10% at the top of the atmosphere. The correction is simply to recalculate the exposure time, by multiplying the exposure time by $1 - f_{DT}$, where f_{DT} is the deadtime fraction. To calculate deadtime fractions, we utilize `hxdtdcor` for Suzaku/PIN. As for the ASCA/GIS and NuSTAR/FPM, we calculated deadtime fractions from the detected count rates by using Figure 18 (specifically, the theoretical prediction for Fast Lorentzian Fit SPREAD-ON, or FLF SP-ON) in Makishima et al. (1996) for ASCA/GIS or Figure 2.7 in Bhalerao (2012) for NuSTAR/FPM, respectively.

Before measuring the atmospheric density, we define unattenuated spectra from the Crab Nebula, i.e., the source spectrum at the top of the Earth's atmosphere, for each occultation data group. To this end, we fit X-ray spectra taken during tangential altitudes well above the atmospheric attenuation with a conventional emission model for the Crab Nebula. The model consists of TBabs \times power-law, where TBabs is the interstellar absorption model (Wilms et al., 2000) and power-law represents the synchrotron radiation from the Crab Nebula. Then, we evaluate lower-altitude X-ray spectra with a spectral model taking account of the effect of the atmospheric absorption. In this procedure, our model is expressed as `vphabs` \times `cabs` \times TBabs \times powerlaw, where `vphabs` and `cabs` represent the photoelectric absorptions and the Compton scattering due to the Earth's atmosphere. In Paper I, we did not consider the `cabs` model. However, the Compton scattering could play an important role in the hard X-ray regime; a total photon cross-section in carbon is dominated by the Compton scattering process in the photon energy range of 0.05–10 MeV (Hubbell et al., 1980). Thus, in this paper, we add it to derive more accurate density profiles especially in the atmosphere below 100-km altitude.

We assume that the atmosphere consists purely of N, O, and Ar, as we did in Paper I. The photon cross-sections per atom are given in Figure 5, where we took the data below and above 1 keV from (Verner et al., 1996) and XCOM (available at <https://physics.nist.gov/PhysRefData/Xcom/html/xcom1.html>), respectively. Given that the density of Ar is $< \sim 0.5\%$ of N, its contribution to the X-ray absorption is so small that we cannot measure its column density. Also, the similarity in cross-sections of N and O does not allow us to measure N and O abundances separately. Therefore, we fix the relative abundances of O/N and Ar/N to model values from NRLMSIS 2.0 (Emmert et al., 2021). We calculate the relative abundances of N, O, and Ar atoms from the MSIS number densities of N_2 , O_2 , O, and Ar, by utilizing a python package `pymphis` available at <https://pypi.org/project/pymphis/>. We assume a single relative abundance pattern calculated at typical parameters, i.e., noon on 2000-09-15, solar radio flux $F_{10.7} = 100$ solar flux unit (SFU, 1 SFU = 10^{-22} W m $^{-2}$ Hz $^{-1}$), geomagnetic index $A_p = 5$. Note that N/O ratios are constant to within 10% below 120 km for various different input parameters to the NRL model and that a combined N and O density varies within $< 1\%$ (see below for more details), which is usually less than the statistical errors. The `cabs` component has a single parameter, i.e., the hydrogen column density, assuming that $N_H \times 1.21 = N_e$ expected for the solar abundance. This is usually good for cosmic plasmas but is not realistic for the air. To adapt `cabs` for the air composition, we compute the total number of protons in the air, i.e., $\sum_i N_i$ with i representing elements N, O, and Ar, Z being the atomic number, N being the column density. Then, we take it as an equivalent hydrogen column density for the input of the `cabs` model. In this calculation, we utilize the abundances of N, O, and Ar obtained from the `vphabs` component, so that the `vphabs` model becomes consistent with the `cabs` model.

The only free parameter in this fitting procedure is the N column density in the atmospheric absorption component `vphabs`. The best-fit N column density and the assumed N/O ratio allow us to calculate a total N + O

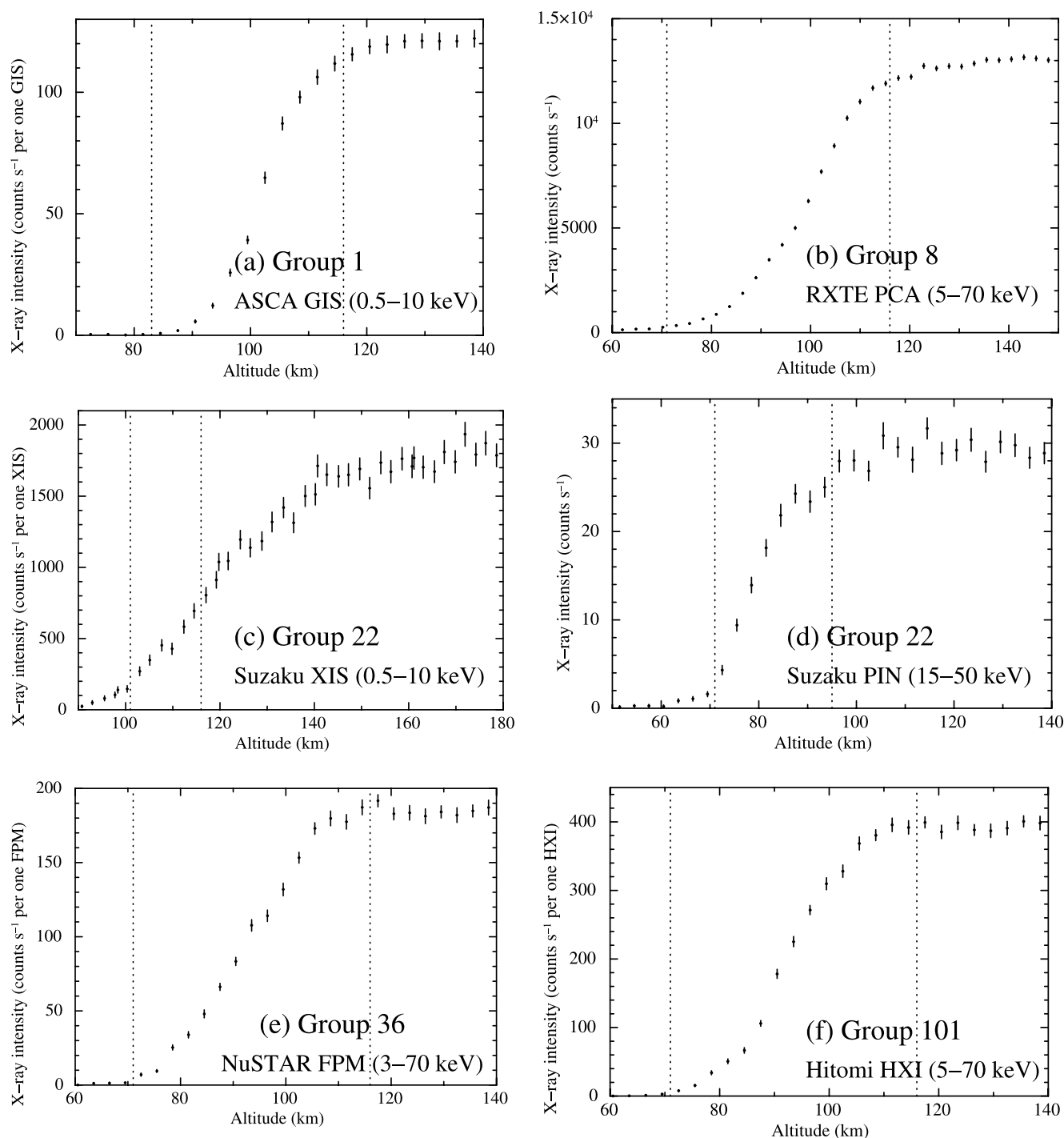


Figure 4. (a) Example occultation light curves for ASCA/GIS. Ten individual occultations in Group 1 (five occultations for GIS2 and GIS3) are merged to improve the photon statistics. The deadtime correction is not performed for this light curve. The altitude range used for our spectral analysis is within dotted vertical lines in each panel. (b)–(f) Same as (a) but for RXTE/PCA, Suzaku/XIS, Suzaku/PIN, NuSTAR/FPM, and Hitomi/HXI. Note that rounded shapes of the light curves are due to gradual changes of the neutral column density as a function of altitude. Also, the altitudes where most of the photons are absorbed vary significantly. This is because energy coverages are different among instruments; photons with higher energies can penetrate more deeply into the atmosphere.

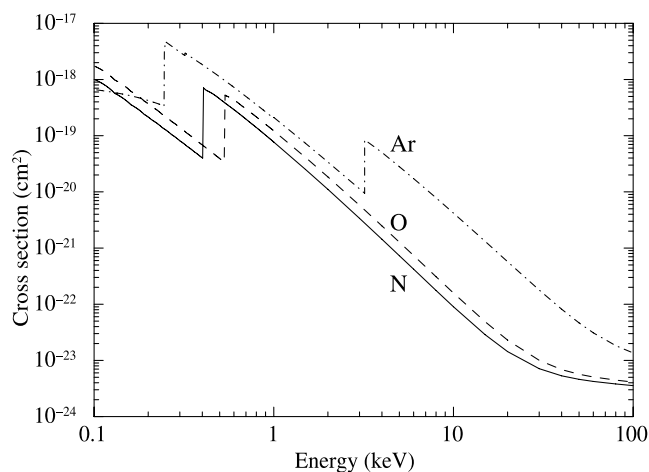


Figure 5. X-ray cross-sections for N, O, and Ar atoms. Solid, dashed, and dash-dotted lines are for N, O, and Ar, respectively.

(molecules and atoms are combined) column density at each altitude layer. All the spectra are well reproduced with this model. Figure 6 shows example spectra with the best-fit models for each of the six instruments.

We evaluate the uncertainties on the N(+O) column density caused by the TLE errors estimated in the previous section. To this end, we reanalyze the six occultations in Obs.ID 70018 obtained with RXTE. We artificially shift the satellite position by $\pm 1\sigma$ in three directions, based on Table 2. From the shifted satellite positions, we recalculate tangent altitudes for each occultation, and remeasure the vertical N + O column density. Thus-derived column density ratios between $+1\sigma$ and -1σ shifts are summarized in Table 3. The total uncertainties in the three directions amount to $\pm 6\%$, which are dominated by longitudinal errors as expected from the TLE errors in Table 2.

The O/N₂ relative abundance in the air is known to vary with season, latitude, and geomagnetic activity (e.g., Meier et al., 2015). Therefore, one may expect variations in the O/N atomic number ratio. Indeed, according to the NRLM-SIS 2.0 model, the variation of O/N is as large as $\pm 10\%$ at 120-km altitude, but is almost negligible below 100 km. To check the maximum effect on the O/N variation, we artificially modify the O/N ratios by $\pm 10\%$, and perform

the spectral fitting. As a result, the combined N + O column density in the air vary by only $\pm 1\%$. This is smaller than typical statistical uncertainties. We note that there is also a possibility of a long-term negative trend in the O/N₂ ratio (Pokhunkov et al., 2009). However, it is currently insignificant, and thus we do not consider the effect of long-term variability in this paper. In any case, the error caused by the incorrect N/O ratio should be smaller than statistical uncertainties, because the magnitude of possible long-term variation is comparable with the short-term variation.

We calculate the local number density at the tangent point by inverting the Abel integral equation (the column density) as we did in Paper I. As a result, we obtain vertical density profiles as a function of geometric altitude. In this inversion process, we arrange the irregular altitude binning for Suzaku/XIS, ~ 0.2 -km bin every ~ 16 km, to become uniform 6-km bins. Then, we generate time series of the N + O density in the time period of 1994–2022 at each altitude. Figure 7 shows combined N + O density trends at each of altitude layers, where we concentrate on the data taken during Autumn-midnight. Note that the temporal coverages by the data are not exactly the same among the plots. This is partly because the sensitive altitudes are different from instrument to instrument (i.e., ASCA/GSI: 83–116 km; NuSTAR/FPM: 71–116 km; Suzaku/XIS: 101–116 km; Suzaku/PIN: 71–95 km; NuSTAR/FPM: 71–116 km; Hitomi/HXI: 71–116 km as shown in Figure 4), and partly because we discard unreliable data with statistical errors of $>20\%$ as they do not help constrain long-term trends.

We then determine long-term trends and solar responses at all altitude layers, by using a multiple linear regression (MLR) model to the N + O density time series. To this end, we utilize a python package `sklearn.linear_model.LinearRegression` developed by Pedregosa et al. (2011). Because we focus on 2 months around spring and autumn equinoxes, our data are inevitably deseasonalized if we perform the MLR fitting for the two seasons separately. The effects of tidal waves (diurnal variations) can be also suppressed by analyzing the data taken around noon and midnight, separately (see Figure 2 and Table A1). Thus, we have four time series of the air density at each altitude. The MLR model is expressed as

$$n_{\text{MLR}}(t) = a + b \times t + c \times F10.7(t),$$

where $n_{\text{MLR}}(t)$ is the N + O density, t is the time (year) when the data were taken, and $F10.7(t)$ is the solar radio flux which is daily averaged at each occultation date; the solar flux data are taken from https://lasp.colorado.edu/lisird/data/noaa_radio_flux and <https://www.spaceweather.gc.ca/forecast-prevision/solar-solaire/solarflux/sx-5-en.php> for old and recent data, respectively. The bottom panel in Figure 7 shows the solar radio (10.7 cm) flux in solar flux unit (SFU). The constant a , long-term trend b , and the amplitude to the solar response c are obtained through least square fitting.

The best-fit long-term trends are summarized in Table 4. The errors quoted are one sigma statistical uncertainties, based on the assumption of independent and identically distributed errors in the fitted data (practically, these

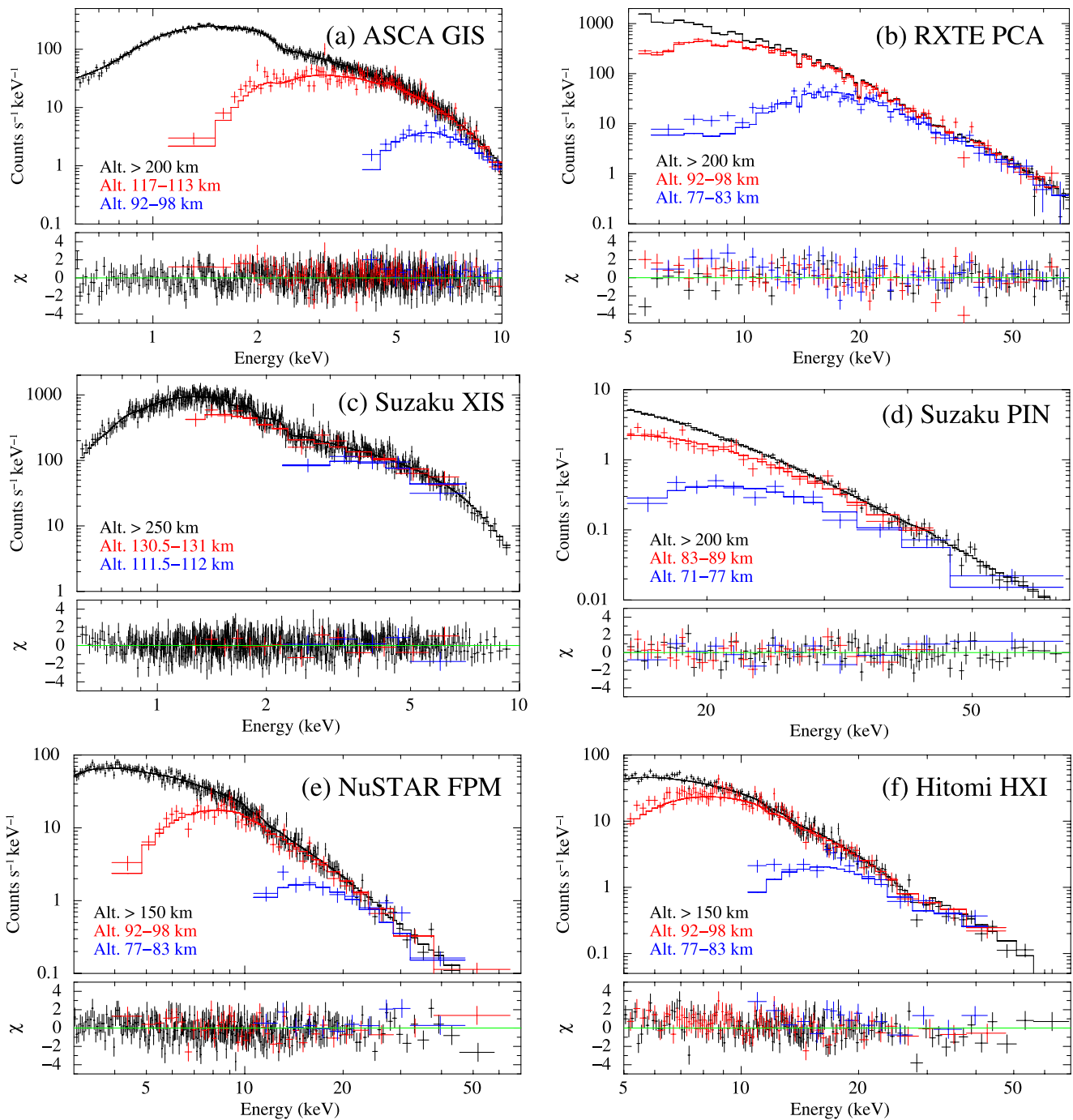


Figure 6. (a) Example X-ray spectra obtained with the ASCA/GIS. The occultations used are the same as Figure 4a. Data in black, red, and blue are taken at different altitude layers. It is clear that the X-ray intensity decreases from the low-energy band, as the layer goes deeper. The data in black are fitted with TBabs \times powerlaw, and those in red and blue are fitted with vphabs \times cabs \times TBabs \times powerlaw (see text for details). Solid lines are the best-fit models. (b)–(f) Same as (a) but for RXTE/PCA, Suzaku/XIS, Suzaku/PIN, NuSTAR/FPM, and Hitomi/HXI.

errors are the “standard error” returned by the python tool). It should be noted that some time series are too sparse (number of data points <4) to derive robust (or unbiased) trends from the MLR fitting, for which we assign “not available (N.A.)” In Figure 7, we plot example best-fit models and the data. The models in this figure are shown for the total (solid) and individual terms, i.e., $a + b \times t$ (dashed) and $c \times F10.7(t)$ (dotted). The density trends obtained are generally negative, which is at least qualitatively consistent with past observations (Bailey et al., 2021; Stober et al., 2014) and numerical simulations (Akmaev et al., 2006; Solomon et al., 2019). There

Table 3
N + O Column Density Errors Caused by 1-sigma TLE Errors

Data group	Ratios of N + O column densities			Total difference
	Longitude	Latitude	Altitude	
	$\frac{N_{A,N+O}(\text{Sat.pos.}-1.1\text{ km})}{N_{A,N+O}(\text{Sat.pos.}+1.1\text{ km})}$	$\frac{N_{A,N+O}(\text{Sat.pos.}-0.17\text{ km})}{N_{A,N+O}(\text{Sat.pos.}+0.17\text{ km})}$	$\frac{N_{A,N+O}(\text{Sat.pos.}-0.1\text{ km})}{N_{A,N+O}(\text{Sat.pos.}+0.1\text{ km})}$	
7	1.12	0.98	0.96	±6%
8	1.13	0.99	0.96	±7%
9	1.11	0.99	0.96	±6%
10	0.89	0.99	0.97	±6%
11	0.89	0.99	0.96	±6%
12	0.88	0.99	0.95	±7%

are no obvious differences among the different seasons and local times. Therefore, we calculated error-weighted means at all altitude layers. Figures 9 left and right show the mean values of the density trends and solar response terms, respectively. The long-term trend is about $-5\%/decade$ throughout the altitudes investigated, except for $\sim 105\text{-km}$ altitude where the trend shows a local minimum of $-12\%/decade$. On the other hand, the solar response term is positive everywhere at about $5\%/100\text{ SFU}$. The positive response to F10.7 is consistent with past observations of the temperature trends in the MLT (e.g., Bailey et al., 2021; Zhang et al., 2016).

To check the goodness of MLR fittings, we calculate χ^2 and reduced- χ^2 values, where $\chi^2 = \sum_{i=1}^n \frac{(Data_i - Model_i)^2}{\sigma_i^2}$, with i being the epoch, n being the number of data points, and σ being one sigma error, and the reduced- χ^2 values are defined as χ^2 divided by the degree of freedom which is the number of data points minus number of free parameters. If the reduced- χ^2 becomes about unity, then we cannot rule out the model (or we can consider that the model is appropriate). In this process, we add TLE-induced 1σ errors on the N + O density, i.e., $\pm 6\%$ as shown in Table 3. Because the TLE-based satellite's positions are used only for ASCA and NuSTAR, we introduce this error only for data taken with the two satellites. Table 5 lists the reduced χ^2 values, from which we can see that the fit quality is mostly satisfactory.

However, there are several poor quality fits, too. They might be improved by introducing additional terms in the MLR model. In fact, Laštovička (2017) summarized several possible drivers of long-term trends in addition to the greenhouse gases. These include secular changes in the geomagnetic activity (Ap) as well as dynamical variations such as Quasi-Biennial Oscillation (QBO), El Nino Southern Oscillation (ENSO), and Arctic Oscillation (AO). In addition, long-term trends in the atmospheric circulation and wave activity may be also important (Wilhelm et al., 2019). Although their effects are not well known, Bailey et al. (2021) tried to incorporate those effects by introducing interhemispheric and intrahemispheric indices calculated from temperature data provided by the National Center for Environmental Prediction/National Center for Atmospheric Research.

Therefore, we perform the MLR fitting by introducing additional terms of Ap (<https://www.gfz-potsdam.de/kp-index>), QBO (https://iridl.ldeo.columbia.edu/SOURCES/Indices/QBO/QBO_realtime/), ENSO (<https://psl.noaa.gov/enso/mei/>), AO (https://www.daculaweather.com/4_ao_index.php), interhemispheric, and intrahemispheric coupling indices. We take the interhemispheric and intrahemispheric coupling indices from Bailey et al. (2021). To see their individual contributions, we perform the MLR fitting by adding each of Ap, QBO, ENSO, AO, and a combination of interhemispheric and intrahemispheric terms to the original model, i.e., linear and solar response terms. Note that the intrahemispheric terms in Bailey et al. (2021) include effects by QBO and ENSO. Therefore, when adding the combination of the interhemispheric and intrahemispheric terms, we effectively take account of several effects at the same time. We realized that none of these additional parameters improve the fit quality. In some cases, the reduced- χ^2 becomes even worse due to the increased number of free parameters. Moreover, we check that the long-term trends and the magnitudes of the solar response remain consistent within the errors before and after introducing the additional terms, which assures the robustness of the result shown in Figure 9. Thus, we conclude that the additional indices do not play an important role in controlling the long-term variation of the neutral density in the MLT region.

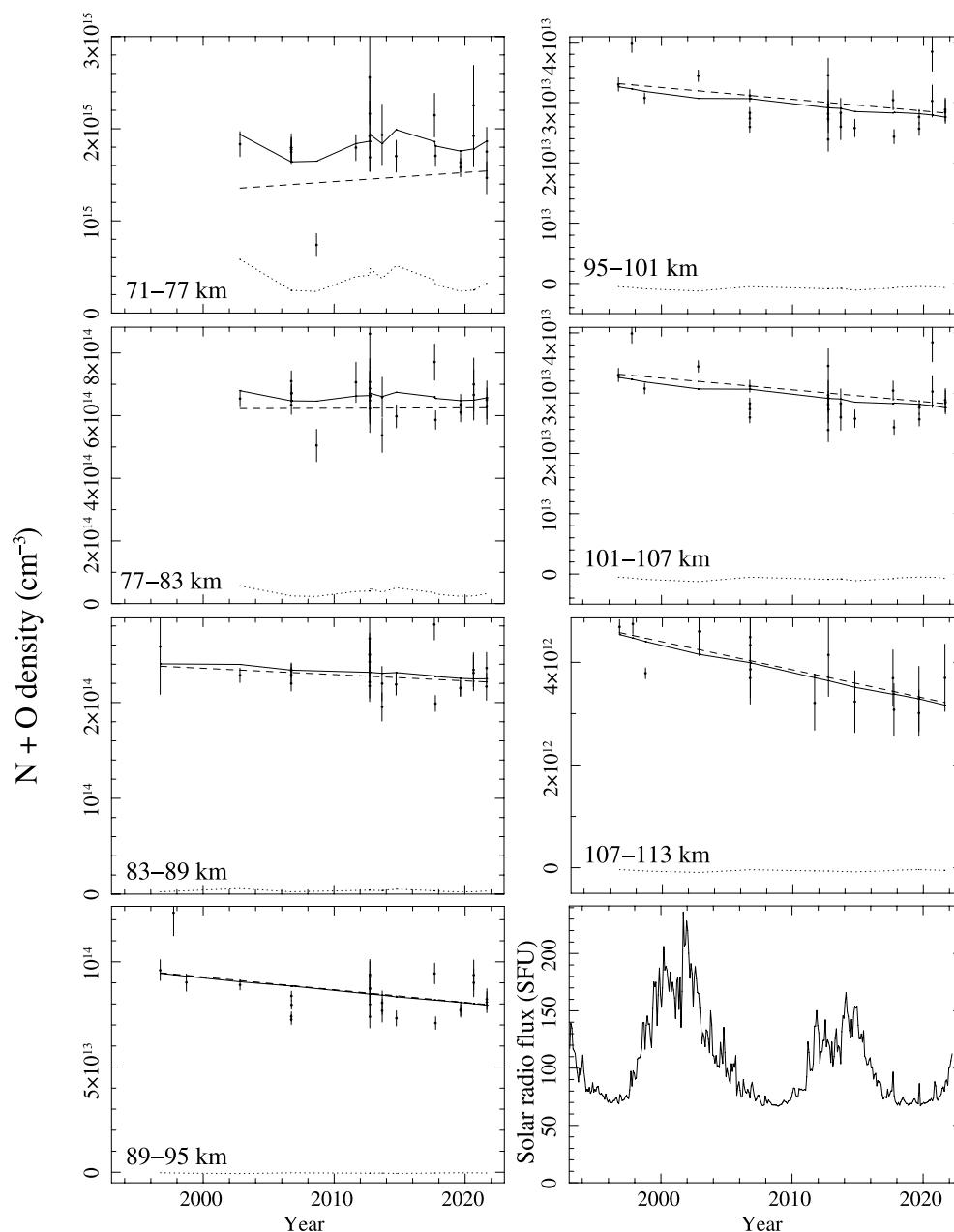


Figure 7. Combined N + O density trends at altitude layers indicated in the lower-left corner of each panel. The plots concentrate on the data taken at Autumn-midnight. The solid lines represent the best-fit model obtained by the multiple linear regression analysis. Individual terms, i.e., $a + b \times t$ and $c \times F10.7(t)$ are also shown as dashed and dotted lines, respectively. The bottom right panel shows the solar radio (10.7 cm) flux in solar flux unit (SFU).

As another effort to interpret the deviation from the long-term density trend, we also search for possible relationships between the residuals and physical parameters. Figure 8 presents data-to-model ratios against such parameters as the latitude, longitude, local time, and day of year, from which we cannot find meaningful patterns.

There are several possibilities to explain the bad fits. One obvious cause is insufficient knowledge of atmospheric wave activities. For example, anomalous short-period gravity waves originating from the lower atmosphere could easily produce outliers in the density time series (e.g., Sato et al., 2018; Yasui et al., 2018). In addition, short-term variations owing to planetary waves, which are often removed by averaging a number of data in a month or two, are difficult to be suppressed in our sparse data sets; we have only a few data groups in one season. In particular, the semidiurnal tide shows a clear solar-cycle dependence (Wilhelm et al., 2019). Another possibility associated

Table 4
Density Trend at Each Altitude Layer

Altitude (km)	Autumn-noon (%/decade)	Autumn-midnight (%/decade)	Spring-noon (%/decade)	Spring-midnight (%/decade)	Mean (%/decade)
71–77	-8.5 ± 5.2	$+5.5 \pm 7.6$	-8.2 ± 8.1	-5.9 ± 9.0	-5.1 ± 3.5
74–80	-7.2 ± 4.1	-0.1 ± 5.5	-6.7 ± 6.6	-3.6 ± 6.7	-4.8 ± 2.7
77–83	-4.0 ± 3.5	$+0.2 \pm 4.3$	$+0.8 \pm 6.1$	-4.7 ± 5.5	-2.3 ± 2.3
80–86	-3.8 ± 3.7	-2.7 ± 4.0	$+3.9 \pm 7.3$	-5.9 ± 5.1	-3.1 ± 2.3
83–89	-4.6 ± 2.8	-2.9 ± 3.0	N.A.	N.A.	-3.8 ± 2.0
86–92	-6.1 ± 2.0	-3.0 ± 2.7	N.A.	N.A.	-4.9 ± 1.6
89–95	-7.4 ± 2.0	-7.1 ± 3.5	N.A.	N.A.	-7.4 ± 1.8
92–98	-7.8 ± 2.2	-5.7 ± 3.5	$+1.1 \pm 8.5$	-3.9 ± 13.9	-6.7 ± 1.8
95–101	-7.9 ± 2.6	-6.6 ± 3.6	-1.0 ± 9.9	-6.9 ± 15.9	-7.2 ± 2.0
98–104	-8.3 ± 2.9	-10.2 ± 3.4	-4.6 ± 10.9	-12.7 ± 16.7	-9.0 ± 2.2
101–107	-9.3 ± 3.4	-14.0 ± 2.7	-6.5 ± 10.9	-1.3 ± 17.6	-11.9 ± 2.0
104–110	-6.3 ± 3.0	-13.4 ± 2.4	$+2.6 \pm 10.0$	-11.3 ± 16.9	-10.1 ± 1.8
107–113	$+2.0 \pm 4.1$	-14.2 ± 3.4	N.A.	$+23.1 \pm 14.0$	-6.5 ± 2.6
110–116	$+4.2 \pm 5.5$	-21.3 ± 6.7	N.A.	N.A.	-6.2 ± 4.3

Note. N.A. stands for not available.

with planetary waves is a stratospheric sudden warming (SSW), which is a sudden temperature increase by more than a few dozen degrees near north pole, caused by a rapid amplification of planetary waves propagating upward from the troposphere (e.g., Matsuno, 1971; Tomikawa et al., 2012). SSW signatures are very small for the latitude band considered here, because it is a primarily polar phenomenon. However, we may not fully rule out the possibility that our data are affected by SSWs. Given that SSWs occur typically in late December to January and early February, we searched for signatures in our data taken in spring. After all, we found no significant density

differences between SSW and non-SSW springs, suggesting that SSWs do not play important roles in our data. Another possible contributor to the bad fits is climatological geophysical variations within the seasonal, local time, latitudinal bins. Such effects could be mitigated by analyzing the data divided by the appropriate model such as MSIS, which will be accounted for in the future work. We should point out, however, that as shown in Figure 8, the data/model ratios do not show clear systematic relationships with any physical parameters examined. This fact suggests that normalization by the MSIS model cannot help improve the MLR fitting quality. Finally, we note that the TLE error is another source that could produce outliers for ASCA and NuSTAR.

4. Discussion

We obtained long-term trends of total number densities of N and O (both atoms and molecules are combined) in the MLT region, based on atmospheric occultations of the Crab Nebula observed with X-ray astronomy satellites, ASCA, RXTE, Suzaku, NuSTAR, and Hitomi. In this section, we compare our results with past observations and numerical simulations.

As we described above, direct density measurements in the MLT region, in particular long-term trends in density, is scarce. As far as we know, the only long-term density trend has been measured for electron densities, which have been measured with sounding rockets for >80 years, providing us with long-term trends (e.g., Friedrich et al., 2017). In general, an increase in the

Table 5
Goodness of MLR Fittings

Altitude (km)	Reduced chi-squares			
	Autumn-noon	Autumn-midnight	Spring-noon	Spring-midnight
71–77	1.705	3.842	0.939	2.364
74–80	1.296	1.157	0.844	0.879
77–83	1.352	1.088	1.226	0.538
80–86	1.493	0.967	1.433	0.544
83–89	1.277	0.817	N.A.	N.A.
86–92	1.131	1.417	N.A.	N.A.
89–95	1.618	5.682	N.A.	N.A.
92–98	1.699	5.710	2.719	2.351
95–101	1.311	3.729	3.112	2.582
98–104	1.228	1.956	2.352	1.745
101–107	1.083	1.075	1.168	1.293
104–110	0.745	0.598	0.610	0.683
107–113	0.755	0.647	N.A.	0.488
110–116	0.641	1.367	N.A.	N.A.

Note. N.A. stands for not available.

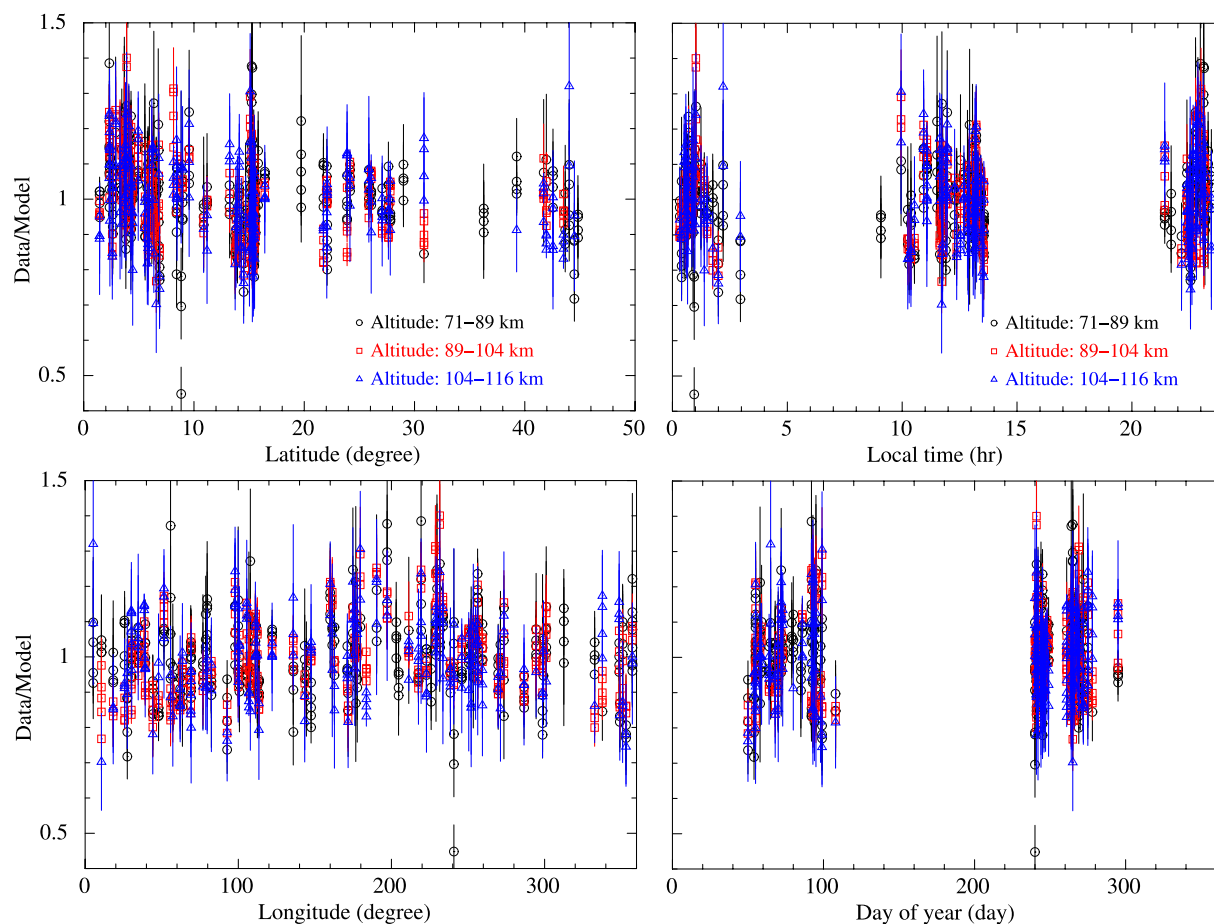


Figure 8. Upper left: Ratios of data to the best-fit multiple linear regression (MLR) model (as shown in Figure 7) as a function of the latitude. Black open circles, red open boxes, and blue open triangles are obtained at tangent altitude ranges of 71–89, 89–104, and 104–116 km, respectively. Lower left, upper right, lower right: Same as upper left, but the x -axes are the longitude, the local time, and the day of year, respectively.

electron density of the order of $\sim 1\%/yr$ was found in the MLT region. This, combined with the vertical increase upward in the electron density, suggests a downward shifts of the electron density profile. This is qualitatively consistent with the atmospheric contraction/descent due to the greenhouse cooling. However, quantitative evaluation of the trend in total density has not yet been obtained.

Except for the electron density, density trends in the MLT region have been inferred from measurements of atmospheric falling from a variety of methods. These include (a) the height of the E -layer's peak electron density (e.g., Bremer, 2008), (b) the mesopause height, i.e., the height at the local temperature minimum (e.g., Yuan et al., 2019), (c) the centroid height of the Na layer (e.g., Clemesha et al., 1997), (d) the meteor peak flux altitude (e.g., Stober et al., 2014), (e) the ionospheric reflection height in the low-frequency (LF) range (e.g., Peters & Entzian, 2015; Peters et al., 2017), (f) the pressure altitude measured by atmospheric occultations and Earth's limb emission (e.g., Bailey et al., 2021). In addition, there are other indirect observables to estimate the atmospheric falling, including the height of the turbopause (Hall et al., 2016; Pokhunkov et al., 2009) and the height of noctilucent clouds, also known as polar mesospheric clouds (e.g., Fiedler et al., 2017; Lübken et al., 2021). In this paper, we do not discuss them, because the turbopause heights are known to be problematic as discussed in Laštovička (2015, 2017) and the altitudes of noctilucent clouds depend not only on the density profile but also strongly depend on the temperature and the water vapor concentration in the atmosphere. Furthermore, there is evidence that space traffic has a strong influence on the interannual variability of the bright noctilucent clouds (Stevens et al., 2022).

The air density corresponds one-to-one to the altitude, given the locally hydrostatic balanced relationship: $d\rho \propto -\rho dh$. Therefore, we can convert the altitude to the density by using some atmospheric models. Consequently, we

Table 6
Altitude → Density Trends in the MLT Region

Target (Method)	Altitude (km)	Obs. period (year)	Altitude trend (km/decade)	Density trend ^a (%/decade)	Reference
<i>E</i> -layer n_c peak height (Ionosonde)	110	1957–2005	-0.029 ± 0.020	$-4.6 \pm 3.2 \pm 0.03$	Bremer (2008)
High mesopause height (Na lidar)	100	1990–2018	-0.45 ± 0.09	$-7.2 \pm 1.4 \pm 0.5$	Yuan et al. (2019)
Meteor peak flux altitude (Specular meteor echo)	92	2002–2014	-0.58 ± 0.01	-5.8 ± 1.1	Stober et al. (2014)
Na layer height (Na lidar)	92	1972–1994	-0.37 ± 0.09	$-6.2 \pm 1.4 \pm 0.4$	Clemesha et al. (1997)
Low mesopause height (Na lidar)	85	1990–2018	-0.13 ± 0.16	$-2.1 \pm 2.6 \pm 0.1$	Yuan et al. (2019)
Radio reflection height (Phase-height experiment)	82	1959–2009	-0.114 ± 0.078	$-1.8 \pm 1.2 \pm 0.01$	Peters et al. (2017)
Pressure altitude (Satellites' remote sensing)	50–91	1991–2020	-0.15 ± 0.05	$-2.4 \pm 0.8 \pm 0.02$	Bailey et al. (2021)

^aThe first and second error terms represent intrinsic measurement errors and possible errors on density gradients ($\pm 1\%/km$) in the empirical models, respectively.

can convert the speed of atmospheric vertical shifts to the rate of density change. According to the NRLMSIS 2.0 model (Emmert et al., 2021), the air density decreases with increasing altitude at a rate of $16 \pm 1\%/km$ in the MLT region. To check possible systematic uncertainties on density models, we also examined another empirical atmospheric density model, Jacchia-Bowman 2008 (Bowman et al., 2008). This model gives a density gradient of $\sim 17\%/km$ at 90-km altitude, which is consistent with the NRLMSIS 2.0 model. Thus, we multiply an altitude trend by a value of $16 \pm 1\%/km$ to derive a density trend. The result is summarized in Table 6 and Figure 7. We note that Stober et al. (2014) showed the density trend inferred from the meteor peak flux altitude, but did not explicitly give the altitude trend. Therefore, we calculated the altitude trend based on Figure 4 in Stober et al. (2014), by performing the same MLR analysis as we did in the previous section. We can see that our measurements are generally consistent with past observations at every altitude.

It should be noted, however, that our trend slopes in density are systematically steeper (albeit within error bars) than those inferred from past observations. Resolving this issue is beyond the scope of this paper, but one problem is that our conversion process from altitude trends to density trends for past observations may be too simple. We also note that the vertical trend profile exhibits a local minimum at ~ 105 km, with a decline rate of $-12\%/decade$. In fact, past observations show the largest (negative maximum) trend near 100 km, which is at least qualitatively consistent with our measurement. Unfortunately, past observations do not cover the altitude range of 100–110 km. Therefore, revealing the density trend in this altitude range is left as an important future work.

The long-term (2–3 decades) density decrease can be also inferred from model comparisons between NRLMSISE-00 and NRLMSIS 2.0, because the former model is based primarily on mass spectrometer data that are now 35–50 years old, whereas the latter one assimilates extensive new (since 2000) measurements and analyses of temperature in the mesosphere, stratosphere, and troposphere, as well as many years of new atomic O and H measurements in the mesosphere. From Figure 18c in Emmert et al. (2021), MSIS 2.0 N_2 densities near 100 km and above are $\sim 20\%$ lower than MSISE-00. This is in reasonable agreement with our result.

As shown in Figure 9 left, our results are also in reasonable agreement with the state-of-the-art numerical simulations using WACCM-eXtended, in which trends are calculated from 5-year simulations for the years 1972–1976 and 2001–2005, which serves as a small ensemble of similar years and are averaged over each of the two ensembles (Solomon et al., 2019). This model takes into account all key trace constituents, i.e., CO_2 , CH_4 (a precursor of H_2O), H_2O , and O_3 . The model was computed for the solar maximum and minimum conditions, the results of which are illustrated in Figure 9 left as the solid and dashed lines, respectively. We can see that the difference

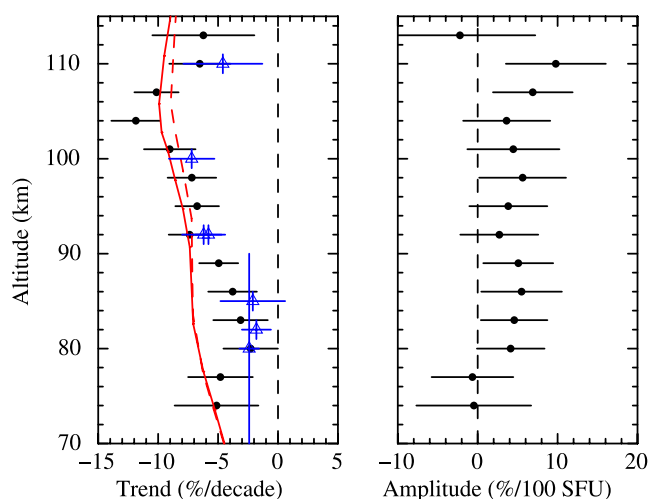


Figure 9. Left: Linear trends in N + O density as a function of geometric altitude. The solid and dashed lines represent numerical simulations computed for the solar maximum and minimum conditions, respectively (Solomon et al., 2019). The triangle data in blue show density trends inferred from past measurements of atmospheric falling. Right: N + O density amplitude to the radio solar flux as a function of geometric altitude.

between the solar minimum and maximum conditions are small in the region of interest. It is interesting to note that numerical experiments exhibit a local maximum of a density decline just above 100 km (the local minimum is more evident in the original figure, Figure 3 in Solomon et al. (2019), showing a wider altitude range). Akmaev et al. (2006) first pointed out that this peak is created by the effects of H₂O and O₃; the cooling effect on the density accumulates with altitude up to ~110 km where in situ H₂O and O₃ forcings disappear. The density trend obtained in this work shows a local (negative) maximum near 105-km altitude. This seems to be the first observational evidence for the local maximum in the density decline due to H₂O and O₃.

There is about 20 years time difference between the simulations by Solomon et al. (2019) and our data sets, which is subject to possible systematic errors, because temporal variations of greenhouse gas concentrations vary from period to period. The simulations took the increasing rates of CO₂, CH₄, and chlorofluorocarbon (sensitive to O₃) to be +4.5%/decade, +6.3%/decade, and +30%/decade, respectively. In the middle and upper stratosphere, H₂O is mainly formed by CH₄ oxidation process. According to Qian et al. (2013), the 6.3% increase in CH₄ concentration results in an increase of 2%/decade in H₂O concentration in the upper atmosphere. This H₂O increase seems to be incorporated in the simulations by Solomon et al. (2019), although it is difficult to evaluate the H₂O increasing rate quantitatively from their paper alone.

Realistic trends of greenhouse gases in the time period of our data (1994–2022) would be different from the values assumed in the simulations by Solomon et al. (2019). In particular, the O₃ trend changed from negative (ozone depletion) to none or positive around 1990 as a consequence of the Montreal protocol in 1987. Because O₃ is a strong absorber of the solar ultraviolet radiation, the temperature (and density) response to O₃ increase is opposite to that of the other major greenhouse gases. The O₃ increase has a heating effect on the MLT region via reduced solar heating, which was demonstrated by numerical simulations by Lübken et al. (2013). Given that O₃ is increasing in the recent three decades (Bernhard & Stierle, 2020; Maillard Barras et al., 2020), O₃ should work to expand the middle and upper atmosphere during the time period of our data sets. Therefore, a proper incorporation of the effect of O₃ in the numerical simulations would make the trend slope in density larger (closer to zero) to some extent.

As for the increasing rate of H₂O concentration, recent measurements of water vapor with the Sounding of the Atmosphere using Broadband Emission Radiometry (SABER) and the Aura Microwave Limb Sounder found a global increase of $3 \pm 1.5\%$ /decade near 80-km altitude (Yue et al., 2019). This is the same level as that assumed in the simulations (likely 2%/decade). Therefore, the simulation is realistic from the point of view of the H₂O concentration.

The CO₂ concentration in the upper atmosphere has been debated (Laštovička & Jelínek, 2019, for a review). However, the most recent result by Rezac et al. (2018) who reanalyzed SABER data between 2002 and 2016 came to a conclusion that CO₂ density trends below 90 km are consistent with the tropospheric value of 5.5%/decade, whereas above 90 km the trend becomes higher, reaching a maximum value of 8.2%/decade at ~105-km altitude for bimonthly time bins (or 10%/decade for monthly time bins). This is consistent with earlier results obtained from the solar occultation data with the Atmospheric Chemistry Experiment Fourier Transform Spectrometer (Emmert et al., 2012). In this context, it seems that the most reliable trend in the MLT is twice larger than the value used in the simulations by Solomon et al. (2019).

In this way, all of these input parameters including CO₂, CH₄, H₂O, and O₃ concentrations must be updated to be consistent with the observational data. Because the density response to the increasing greenhouse gases is nonlinear, it is necessary to perform numerical simulations that use physical parameters consistent with observational data.

5. Conclusions

We obtained long-term density trends in the last 28 years (1994–2022) of the Earth's upper atmosphere at geometric altitudes between 71 and 116 km with a resolution of 3 km, based on atmospheric occultations of the Crab Nebula observed with X-ray astronomy satellites, ASCA, RXTE, Suzaku, NuSTAR, and Hitomi. The data taken in different seasons (spring and autumn) and different local times (noon and midnight) are combined to provide a single vertical profile of trend slopes. The density trends are overall negative at roughly -5% /decade. This is roughly consistent with inferences from past measurements of the rates of settling atmosphere in the MLT region. In the 100–110-km altitude, we found an exceptionally high density decline of about -12% /decade. We believe that this peak is the first observational evidence for strong cooling due to water vapor and ozone near 110 km, which was first identified in a numerical simulation by Akmaev et al. (2006). However, this feature needs to be verified by further observations as well as numerical simulations, which use physical parameters that correspond to the time periods of observations.

Appendix A: Summary of Atmospheric Occultations Analyzed

All the data analyzed in this paper are listed in Table A1. For ASCA and NuSTAR, we recalculated satellites' positions to improve the accuracy, using the skyfield package into which we gave orbital elements taken from NORAD TLEs (<http://celestrak.com/NORAD/archives/request.php>) with the SGP4 propagator algorithm. We use original positions for the other satellites, which are provided by the teams. These satellite positions are the most important ingredients to determine tangent altitudes and tangent points. We collected data taken in spring (± 30 days around the equinox) and autumn (± 30 days around the equinox). We also limit the data taken in the northern hemisphere. The last column denotes the data group. We merge the data in the same group for our spectral analysis.

Table A1
Atmospheric Occultations of the Crab Nebula Analyzed in This Paper

Instrument	UT ^a	Tangent point ^b	Local time ^c	Type	Group
(Obs.ID)	(HH:MM:SS)	Long, lat (°)	(HH:MM:SS)		
ASCA/GIS (10010180)	1994-09-28, 05:24:41	106.9204, 41.9572	12:32:21	Setting	1
	1994-09-28, 14:59:35	322.4569, 41.5094	12:29:24	Setting	1
	1994-09-29, 00:34:29	177.9692, 41.0303	12:26:21	Setting	1
	1994-09-29, 02:10:18	153.8861, 40.9471	12:25:50	Setting	1
	1994-09-29, 05:21:56	105.7188, 40.7777	12:24:47	Setting	1
ASCA/GIS (10010190)	1994-10-04, 13:07:13	337.7223, 30.8591	11:38:05	Setting	2
	1994-10-04, 22:42:08	193.0689, 29.9003	11:34:23	Setting	2
	1994-10-05, 00:17:58	168.9556, 29.7475	11:33:47	Setting	2
	1994-10-05, 01:53:47	144.8492, 29.5808	11:33:10	Setting	2
	1994-10-05, 03:29:36	120.7376, 29.4155	11:32:33	Setting	2
	1994-10-05, 09:52:53	24.2916, 28.7546	11:30:02	Setting	2
	1994-10-05, 11:28:42	0.1818, 28.5844	11:29:25	Setting	2
	1994-10-05, 13:04:31	336.0716, 28.4137	11:28:48	Setting	2
ASCA/GIS (10403000)	1996-09-17, 08:18:21	211.3219, 41.7094	22:23:38	Rising	3
	1996-09-17, 09:23:55	38.5445, 6.2673	11:58:05	Setting	4
	1996-09-17, 09:54:07	187.4372, 41.5528	22:23:51	Rising	3
	1996-09-17, 10:59:44	14.6868, 6.6670	11:58:27	Setting	4
	1996-09-17, 11:29:52	163.5178, 41.4414	22:23:56	Rising	3
	1996-09-17, 23:46:12	183.7813, 9.6564	12:01:18	Setting	4

Table A1
Continued

Instrument	UT ^a	Tangent point ^b	Local time ^c	Type	Group	
(Obs.ID)	(HH:MM:SS)	Long, lat (°)	(HH:MM:SS)			
ASCA/GIS (11501000)	1997-09-26, 07:45:40	228.6920, 8.1441	23:00:25	Rising	5	
	1997-09-26, 09:21:21	204.6166, 8.3629	22:59:48	Rising	5	
	1997-09-26, 15:44:06	108.2979, 9.2428	22:57:16	Rising	5	
ASCA/GIS (11602000)	1998-09-15, 10:12:57	183.6161, 43.5114	22:27:24	Rising	6	
	1998-09-15, 11:48:28	159.6453, 43.5447	22:27:02	Rising	6	
	1998-09-15, 13:24:00	135.7008, 43.5384	22:26:48	Rising	6	
	1998-09-16, 11:41:20	160.3667, 43.6404	22:22:47	Rising	6	
	1998-09-16, 14:52:23	112.4787, 43.6316	22:22:17	Rising	6	
	1998-09-16, 14:52:23	112.4787, 43.6316	22:22:17	Rising	6	
RXTE/PCA (70018)	2002-03-05, 14:05:26	171.2213, 27.0653	01:30:19	Setting	7	
	2002-08-29, 22:14:21	222.8523, 1.4405	13:05:44	Setting	8	
	2002-09-26, 02:04:09	147.4954, 22.0718	11:54:06	Setting	9	
	2002-10-22, 14:23:43	105.4934, 3.7893	21:25:41	Rising	10	
	2003-02-27, 04:33:13	122.0489, 16.4205	12:41:23	Rising	11	
	2003-03-27, 03:39:21	111.3536, 8.4639	11:04:45	Rising	12	
RXTE/PCA (92018)	2006-09-03, 21:09:40	245.9062, 27.8003	13:33:16	Setting	13	
	2006-09-04, 20:43:57	250.4656, 26.0700	13:25:47	Setting	14	
	2006-09-05, 20:18:14	254.9570, 24.1404	13:18:02	Setting	15	
	2006-09-06, 19:52:32	259.3940, 22.0419	13:10:05	Setting	16	
	2006-09-23, 21:05:07	25.7248, 21.7392	22:48:00	Rising	17	
	2006-09-24, 20:39:22	30.1601, 23.8829	22:40:00	Rising	18	
	2006-09-25, 20:13:36	34.6437, 25.8576	22:32:09	Rising	19	
	2006-09-26, 19:47:50	39.1949, 27.6340	22:24:36	Rising	20	
	Suzaku/XIS + PIN (100023010)	2005-09-15, 15:47:27	112.9348, 21.6094	23:19:10	Rising	21
		2005-09-15, 17:23:23	88.7894, 21.8078	23:18:32	Rising	21
2005-09-15, 18:59:19		64.6462, 22.0065	23:17:53	Rising	21	
PIN only	2005-09-15, 14:11:30	117.5 154.0	23:19:50	Rising	21	
Suzaku/XIS + PIN (100023020)	2005-09-15, 20:35:15	40.5040, 22.2049	23:17:15	Rising	21	
	2005-09-16, 01:23:04	328.0701, 22.7902	23:15:20	Rising	21	
Suzaku/XIS + PIN (102019010)	2007-03-20, 11:03:59	203.0962, 28.9984	00:36:21	Setting	22	
	2007-03-20, 19:03:28	82.4316, 28.1415	00:33:11	Setting	22	
	2007-03-20, 20:39:21	58.3004, 27.9608	00:32:32	Setting	22	
	2007-03-20, 22:15:15	34.1662, 27.7856	00:31:54	Setting	22	
	2007-03-20, 23:51:09	10.0323, 27.6087	00:31:15	Setting	22	
	2007-03-21, 01:27:03	345.9020, 27.4311	00:30:38	Setting	22	
	2007-03-21, 03:02:56	321.7692, 27.2496	00:30:00	Setting	22	
	2007-03-21, 04:38:50	297.6363, 27.0733	00:29:21	Setting	22	
	2007-03-21, 06:14:44	273.5048, 26.8952	00:28:45	Setting	22	
	2007-03-21, 07:50:38	249.3681, 26.7177	00:28:05	Setting	22	
	2007-03-21, 09:26:31	225.2351, 26.5324	00:27:27	Setting	22	
	PIN only	2007-03-20, 12:39:53	178.9600, 28.8299	00:35:43	Setting	22
		2007-03-20, 14:15:47	154.8306, 28.6595	00:35:05	Setting	22
2007-03-20, 15:51:40		130.6976, 28.4824	00:34:27	Setting	22	

Table A1
Continued

Instrument (Obs.ID)	UT ^a (HH:MM:SS)	Tangent point ^b Long, lat (°)	Local time ^c (HH:MM:SS)	Type	Group
Suzaku/XIS + PIN (103007010)	2007-03-20, 17:27:34	106.5661, 28.3117	00:33:48	Setting	22
	2007-03-21, 11:02:25	201.1047, 26.3490	00:26:49	Setting	22
	2007-03-21, 12:38:19	176.9683, 26.1683	00:26:11	Setting	22
	2008-08-27, 08:53:45	240.7545, 8.8327	00:56:45	Rising	23
	2008-08-27, 10:29:38	216.6275, 9.0504	00:56:08	Rising	23
	2008-08-27, 12:05:31	192.5022, 9.2686	00:55:31	Rising	23
	2008-08-27, 13:41:25	168.3694, 9.4947	00:54:52	Rising	23
	2008-08-27, 15:17:18	144.2389, 9.7116	00:54:15	Rising	23
	2008-08-27, 16:53:11	120.1106, 9.9297	00:53:36	Rising	23
	2008-08-27, 18:29:05	95.9780, 10.1570	00:52:59	Rising	23
	2008-08-27, 20:04:58	71.8479, 10.3754	00:52:21	Rising	23
2008-08-27, 21:40:51	47.7197, 10.5942	00:51:42	Rising	23	
Suzaku/PIN (only) (104001010)	2008-08-28, 04:04:24	311.2021, 11.4750	00:49:11	Rising	23
	2009-04-02, 02:28:52	312.5537, 15.8190	23:19:04	Setting	24
	2009-04-02, 05:40:37	264.3008, 15.3940	23:17:48	Setting	24
	2009-04-02, 07:16:29	240.1773, 15.1828	23:17:11	Setting	24
	2009-04-02, 08:52:22	216.0431, 14.9684	23:16:32	Setting	24
	2009-04-02, 10:28:15	191.9123, 14.7529	23:15:52	Setting	24
	2009-04-02, 12:04:08	167.7842, 14.5363	23:15:15	Setting	24
	2009-04-02, 13:40:00	143.6593, 14.3257	23:14:38	Setting	24
	2009-04-02, 15:15:53	119.5299, 14.1091	23:13:59	Setting	24
	2009-04-02, 16:51:45	95.4068, 13.8977	23:13:22	Setting	24
	2009-04-02, 18:27:38	71.2755, 13.6801	23:12:43	Setting	24
2009-04-02, 20:03:31	47.1460, 13.4604	23:12:06	Setting	24	
2009-04-02, 21:39:24	23.0145, 13.2414	23:11:26	Setting	24	
2009-04-02, 23:15:16	358.8897, 13.0297	23:10:49	Setting	24	
Suzaku/XIS + PIN (104001070)	2009-04-03, 00:51:09	334.7635, 12.8104	23:10:12	Setting	24
	2010-02-23, 01:07:24	27.5234, 44.5019	02:57:29	Setting	25
	2010-02-23, 02:43:15	3.4639, 44.4581	02:57:06	Setting	25
	2010-02-23, 04:19:07	339.4214, 44.4512	02:56:48	Setting	25
	2010-02-23, 05:54:58	315.3504, 44.4045	02:56:21	Setting	25
	2010-02-23, 13:54:14	195.0371, 44.2031	02:54:21	Setting	25
	2010-02-23, 15:30:05	170.9671, 44.1518	02:53:57	Setting	25
	2010-02-23, 17:05:56	146.8931, 44.0990	02:53:30	Setting	25
	2010-02-23, 18:41:48	122.8454, 44.0821	02:53:09	Setting	25
	2010-02-23, 20:17:39	98.7736, 44.0294	02:52:44	Setting	25
	2010-02-23, 21:53:30	74.6982, 43.9783	02:52:17	Setting	25
2010-02-23, 23:29:21	50.6253, 43.9263	02:51:51	Setting	25	
Suzaku/XIS + PIN (105002010)	2010-02-24, 01:05:12	26.5563, 43.8720	02:51:24	Setting	25
	2010-02-24, 02:41:03	2.4805, 43.8172	02:50:57	Setting	25
	2010-02-24, 04:16:54	338.4038, 43.7578	02:50:30	Setting	25
	2010-04-06, 00:13:27	132.5794, 44.7686	09:03:46	Rising	26

Table A1
Continued

Instrument	UT ^a	Tangent point ^b	Local time ^c	Type	Group
(Obs.ID)	(HH:MM:SS)	Long, lat (°)	(HH:MM:SS)		
PIN only	2010-04-06, 01:49:18	108.5461, 44.7772	09:03:29	Rising	26
	2010-04-06, 03:25:10	84.5450, 44.7403	09:03:20	Rising	26
	2010-04-06, 05:01:02	60.5457, 44.6994	09:03:11	Rising	26
	2010-04-06, 06:36:54	36.5486, 44.6582	09:03:05	Rising	26
	2010-04-06, 08:12:45	12.5208, 44.6633	09:02:48	Rising	26
	2010-04-06, 09:48:37	348.5188, 44.6257	09:02:40	Rising	26
	2010-04-05, 16:14:09	252.6709, 44.8427	09:04:50	Rising	26
	2010-04-05, 17:50:00	228.6303, 44.8519	09:04:31	Rising	26
	2010-04-05, 19:25:52	204.6280, 44.8210	09:04:22	Rising	26
	2010-04-05, 21:01:43	180.5906, 44.8324	09:04:04	Rising	26
Suzaku/XIS + PIN (105029010)	2010-04-05, 22:37:35	156.5839, 44.8016	09:03:55	Rising	26
	2011-03-21, 19:41:41	78.7092, 39.2653	00:56:30	Setting	27
	2011-03-21, 21:17:33	54.7942, 39.4346	00:56:43	Setting	27
	2011-03-21, 22:53:25	30.8867, 39.6003	00:56:57	Setting	27
	2011-03-22, 00:29:18	7.0040, 39.8187	00:57:17	Setting	27
	2011-03-22, 02:05:10	343.0985, 39.9859	00:57:33	Setting	27
	2011-03-22, 03:41:02	319.1887, 40.1518	00:57:47	Setting	27
	2011-03-22, 05:16:54	295.2737, 40.3134	00:57:59	Setting	27
	2011-03-22, 10:04:30	223.5321, 40.7892	00:58:36	Setting	27
	2011-03-22, 11:40:22	199.6170, 40.9492	00:58:50	Setting	27
	2011-03-22, 13:16:13	175.6760, 41.0566	00:58:54	Setting	27
	2011-03-22, 14:52:05	151.7591, 41.2150	00:59:07	Setting	27
	2011-03-22, 16:27:57	127.8495, 41.3677	00:59:20	Setting	27
	2011-03-22, 18:03:48	103.9000, 41.4732	00:59:23	Setting	27
	2011-03-22, 19:39:40	79.9866, 41.6262	00:59:35	Setting	27
	2011-03-22, 21:15:32	56.0717, 41.7799	00:59:48	Setting	27
	2011-03-22, 22:51:23	32.1257, 41.8849	00:59:53	Setting	27
	2011-03-23, 00:27:15	8.2138, 42.0381	01:00:06	Setting	27
	2011-03-23, 02:03:06	344.2684, 42.1442	01:00:10	Setting	27
	Suzaku/XIS + PIN (106012010)	2011-09-01, 06:39:28	252.0472, 42.5591	23:27:38	Rising
2011-09-01, 07:45:03		79.6606, 5.5418	13:03:41	Setting	29
2011-09-01, 08:15:17		228.0969, 42.4752	23:27:39	Rising	28
2011-09-01, 09:51:07		204.1749, 42.3442	23:27:47	Rising	28
2011-09-01, 10:56:49		31.8986, 6.3004	13:04:23	Setting	29
2011-09-01, 11:26:56		180.2215, 42.2622	23:27:48	Rising	28
2011-09-01, 13:02:46		156.3045, 42.1316	23:27:59	Rising	28
2011-09-01, 14:38:36		132.3875, 41.9985	23:28:08	Rising	28
2011-09-01, 16:14:26		108.4658, 41.8605	23:28:17	Rising	28
2011-09-01, 17:50:15		84.5215, 41.7703	23:28:19	Rising	28
2011-09-01, 19:26:05		60.6072, 41.6296	23:28:30	Rising	28
2011-09-01, 20:32:07		248.6250, 8.5945	13:06:37	Setting	29
2011-09-01, 21:01:55	36.6872, 41.4873	23:28:38	Rising	28	

Table A1
Continued

Instrument (Obs.ID)	UT ^a (HH:MM:SS)	Tangent point ^b Long, lat (°)	Local time ^c (HH:MM:SS)	Type	Group
	2011-09-01, 22:08:00	224.7420, 8.9729	13:06:57	Setting	29
	2011-09-01, 22:37:45	12.7723, 41.3508	23:28:50	Rising	28
	2011-09-01, 23:43:53	200.8643, 9.3497	13:07:19	Setting	29
	2011-09-02, 00:13:35	348.8518, 41.2116	23:28:59	Rising	28
	2011-09-02, 01:19:46	176.9834, 9.7286	13:07:41	Setting	29
	2011-09-02, 02:55:40	153.1248, 10.1580	13:08:08	Setting	29
	2011-09-02, 04:31:33	129.2479, 10.5358	13:08:31	Setting	29
	2011-09-02, 06:07:26	105.3699, 10.9140	13:08:53	Setting	29
Suzaku/XIS + PIN (106014010)	2012-03-14, 01:27:52	348.9473, 21.5192	00:43:39	Setting	30
	2012-03-14, 03:03:35	324.8601, 21.3204	00:43:00	Setting	30
	2012-03-14, 04:39:18	300.7737, 21.1207	00:42:23	Setting	30
	2012-03-14, 06:15:01	276.6836, 20.9213	00:41:44	Setting	30
	2012-03-14, 07:50:44	252.5936, 20.7208	00:41:06	Setting	30
	2012-03-14, 09:26:27	228.5048, 20.5185	00:40:27	Setting	30
	2012-03-14, 11:02:10	204.4156, 20.3156	00:39:48	Setting	30
	2012-03-14, 12:37:53	180.3265, 20.1133	00:39:11	Setting	30
	2012-03-14, 14:13:36	156.2397, 19.9099	00:38:32	Setting	30
	2012-03-14, 15:49:19	132.1504, 19.7072	00:37:54	Setting	30
	2012-03-14, 17:25:02	108.0625, 19.5037	00:37:15	Setting	30
	2012-03-14, 19:00:45	83.9744, 19.2992	00:36:38	Setting	30
	2012-03-14, 20:36:28	59.8841, 19.0937	00:36:00	Setting	30
	2012-03-14, 22:12:11	35.7953, 18.8861	00:35:21	Setting	30
Suzaku/XIS + PIN (107011010)	2012-09-26, 06:38:44	225.9450, 43.6655	21:42:29	Rising	31
	2012-09-26, 08:14:24	201.9427, 43.6907	21:42:10	Rising	31
	2012-09-26, 09:50:03	177.9161, 43.7499	21:41:42	Rising	31
	2012-09-26, 11:25:42	153.8869, 43.8101	21:41:13	Rising	31
	2012-09-26, 13:01:22	129.8874, 43.8355	21:40:54	Rising	31
	2012-09-26, 14:37:01	105.8578, 43.8916	21:40:26	Rising	31
	2012-09-26, 16:12:40	81.8353, 43.9488	21:40:00	Rising	31
	2012-09-26, 17:48:19	57.8115, 44.0017	21:39:33	Rising	31
	2012-09-26, 19:23:59	33.8157, 44.0155	21:39:14	Rising	31
	2012-09-26, 20:59:38	9.7952, 44.0657	21:38:48	Rising	31
	2012-09-26, 22:35:17	345.7727, 44.1193	21:38:21	Rising	31
	2012-09-27, 04:57:55	249.7428, 44.2478	21:36:52	Rising	31
Suzaku/XIS + PIN (107012010)	2013-02-27, 01:09:14	176.7227, 6.7619	12:56:07	Rising	32
	2013-02-27, 02:44:51	152.6637, 6.9839	12:55:30	Rising	32
	2013-02-27, 04:20:28	128.6018, 7.2055	12:54:51	Rising	32
	2013-02-27, 05:56:05	104.5407, 7.4277	12:54:14	Rising	32
	2013-02-27, 07:31:42	80.4816, 7.6515	12:53:36	Rising	32
	2013-02-27, 09:07:19	56.4198, 7.8743	12:52:59	Rising	32
	2013-02-27, 17:05:23	296.1170, 8.9776	12:49:50	Rising	32
	2013-02-27, 18:41:00	272.0577, 9.2017	12:49:13	Rising	32

Table A1
Continued

Instrument	UT ^a	Tangent point ^b	Local time ^c	Type	Group	
(Obs.ID)	(HH:MM:SS)	Long, lat (°)	(HH:MM:SS)			
PIN only	2013-02-27, 20:16:37	247.9946, 9.4233	12:48:34	Rising	32	
	2013-02-27, 21:52:14	223.9340, 9.6449	12:47:57	Rising	32	
Suzaku/XIS + PIN (108011010)	2013-09-30, 11:41:53	357.3104, 19.7266	11:31:06	Setting	33	
	2013-09-30, 13:17:25	333.2719, 19.5224	11:30:29	Setting	33	
	2013-09-30, 14:52:57	309.2295, 19.3195	11:29:52	Setting	33	
	2013-09-30, 16:28:29	285.1842, 19.1169	11:29:12	Setting	33	
	2013-09-30, 18:04:01	261.1428, 18.9115	11:28:35	Setting	33	
	2013-09-30, 19:39:34	237.0956, 18.7033	11:27:56	Setting	33	
	2013-09-30, 21:15:06	213.0517, 18.4971	11:27:18	Setting	33	
	2013-09-30, 22:50:38	189.0108, 18.2901	11:26:39	Setting	33	
	2013-10-01, 00:26:10	164.9684, 18.0839	11:26:02	Setting	33	
	2013-10-01, 02:01:42	140.9276, 17.8767	11:25:23	Setting	33	
	2013-10-01, 03:37:15	116.8792, 17.6673	11:24:46	Setting	33	
	2013-10-01, 05:12:47	92.8361, 17.4602	11:24:06	Setting	33	
	2013-10-01, 06:48:19	68.7952, 17.2506	11:23:29	Setting	33	
	2013-10-01, 08:23:51	44.7519, 17.0404	11:22:50	Setting	33	
PIN only	2013-10-01, 09:59:23	20.7104, 16.8293	11:22:13	Setting	33	
Suzaku/XIS + PIN (108012010)	2014-03-06, 01:51:23	5.2762, 44.0279	02:12:29	Setting	34	
	2014-03-06, 03:26:48	341.3101, 43.9703	02:12:02	Setting	34	
	2014-03-06, 05:02:14	317.3638, 43.9483	02:11:40	Setting	34	
	2014-03-06, 12:59:21	197.5711, 43.7266	02:09:38	Setting	34	
	2014-03-06, 14:34:46	173.6008, 43.6648	02:09:10	Setting	34	
	2014-03-06, 16:10:11	149.6319, 43.5993	02:08:42	Setting	34	
	2014-03-06, 17:45:37	125.6839, 43.5707	02:08:21	Setting	34	
	2014-03-06, 19:21:02	101.7124, 43.5079	02:07:51	Setting	34	
	2014-03-06, 20:56:28	77.7640, 43.4797	02:07:31	Setting	34	
	2014-03-06, 22:31:53	53.7919, 43.4175	02:07:03	Setting	34	
	2014-03-07, 00:07:18	29.8190, 43.3556	02:06:33	Setting	34	
	NuSTAR/FPM (10013021002)	2012-09-20, 03:14:44	299.2689, 15.5307	23:11:48	Rising	35
		2012-09-20, 04:16:38	112.4618, 5.5680	11:46:27	Setting	36
		2012-09-20, 04:51:46	274.9422, 15.5296	23:11:31	Rising	35
2012-09-20, 05:53:41		88.1595, 5.6261	11:46:18	Setting	36	
NuSTAR/FPM (10013024002)	2012-09-20, 11:19:56	177.6637, 15.4670	23:10:35	Rising	37	
	2012-09-20, 12:21:52	350.9328, 5.8355	11:45:34	Setting	38	
	2012-09-20, 12:56:58	153.3413, 15.4654	23:10:18	Rising	37	
	2012-09-20, 13:58:54	326.6212, 5.8660	11:45:23	Setting	38	
NuSTAR/FPM (10013022002)	2012-09-20, 19:25:08	55.7379, 15.3000	23:08:04	Rising	39	
	2012-09-20, 20:27:05	229.0669, 6.1742	11:43:21	Setting	40	
	2012-09-20, 21:02:10	31.4155, 15.2962	23:07:49	Rising	39	
	2012-09-20, 22:04:08	204.7604, 6.2364	11:43:09	Setting	40	
NuSTAR/FPM (10013022004)	2012-09-21, 03:30:20	294.4665, 15.3093	23:08:11	Rising	41	
	2012-09-21, 04:32:19	107.8726, 6.3589	11:43:48	Setting	42	

Table A1
Continued

Instrument	UT ^a	Tangent point ^b	Local time ^c	Type	Group
(Obs.ID)	(HH:MM:SS)	Long, lat (°)	(HH:MM:SS)		
NuSTAR/FPM (10013022006)	2012-09-21, 05:07:22	270.1443, 15.3033	23:07:55	Rising	41
	2012-09-21, 06:09:22	83.5663, 6.4222	11:43:36	Setting	42
	2012-09-21, 16:26:39	99.9226, 15.1632	23:06:20	Rising	43
NuSTAR/FPM (80001022002)	2012-09-21, 18:03:42	75.6101, 15.1242	23:06:07	Rising	43
	2013-03-09, 07:46:38	68.9599, 2.5936	12:22:27	Rising	44
	2013-03-09, 08:48:05	240.6845, 14.6767	00:50:48	Setting	45
	2013-03-09, 09:23:38	44.6454, 2.5835	12:22:11	Rising	44
	2013-03-09, 10:25:05	216.3539, 14.6495	00:50:29	Setting	45
NuSTAR/FPM (10013037002)	2013-03-09, 11:00:39	20.3403, 2.5505	12:22:00	Rising	44
	2013-03-09, 12:02:05	192.0277, 14.6201	00:50:11	Setting	45
	2013-04-03, 09:09:49	18.2802, 15.0293	10:22:55	Rising	46
	2013-04-03, 10:11:17	190.2760, 2.8922	22:52:23	Setting	47
NuSTAR/FPM (10013037004)	2013-04-03, 10:46:49	353.9586, 15.0456	10:22:38	Rising	46
	2013-04-03, 11:48:17	165.9694, 2.9140	22:52:09	Setting	47
	2013-04-04, 11:01:45	349.1032, 15.3330	10:18:09	Rising	48
NuSTAR/FPM (10013037006)	2013-04-04, 12:03:17	161.3774, 3.2953	22:48:47	Setting	49
	2013-04-04, 12:38:45	324.7830, 15.3422	10:17:52	Rising	48
	2013-04-04, 13:40:17	137.0754, 3.3221	22:48:34	Setting	49
	2013-04-05, 06:25:42	57.2489, 15.4965	10:14:40	Rising	50
	2013-04-05, 07:27:18	229.7341, 3.6801	22:46:14	Setting	51
NuSTAR/FPM (10013038002)	2013-04-05, 08:02:42	32.9296, 15.5003	10:14:25	Rising	50
	2013-04-05, 09:04:18	205.4322, 3.7116	22:46:00	Setting	51
	2013-04-08, 12:01:33	330.1119, 15.4659	10:01:59	Rising	52
	2013-04-08, 13:03:25	143.3684, 5.7677	22:36:52	Setting	53
NuSTAR/FPM (10013038004)	2013-04-08, 13:38:33	305.8007, 15.4487	10:01:45	Rising	52
	2013-04-08, 14:40:25	119.0723, 5.8124	22:36:42	Setting	53
	2013-04-09, 21:58:31	179.6391, 15.0960	09:57:03	Rising	54
NuSTAR/FPM (10013037008)	2013-04-09, 23:00:29	353.1661, 6.8803	22:33:07	Setting	55
	2013-04-09, 23:35:31	155.3323, 15.0710	09:56:49	Rising	54
	2013-04-10, 00:37:29	328.8659, 6.9306	22:32:56	Setting	55
	2013-04-18, 09:40:41	357.8577, 9.2175	09:32:06	Rising	56
	2013-04-18, 10:42:49	171.7134, 13.7309	22:09:39	Setting	57
NuSTAR/FPM (10002001002)	2013-04-18, 11:17:41	333.5635, 9.1638	09:31:55	Rising	56
	2013-04-18, 12:19:49	147.4151, 13.7684	22:09:28	Setting	57
	2013-09-02, 04:29:03	298.6616, 15.4632	00:23:40	Rising	58
	2013-09-02, 05:30:37	111.1456, 3.6867	12:55:10	Setting	59
NuSTAR/FPM (10002001004)	2013-09-02, 06:06:01	274.3493, 15.4756	00:23:24	Rising	58
	2013-09-02, 07:07:35	86.8473, 3.7114	12:54:57	Setting	59
	2013-09-03, 06:20:32	269.6793, 15.5823	00:19:14	Rising	60
	2013-09-03, 07:22:11	82.4347, 4.2782	12:51:55	Setting	61
	2013-09-03, 07:57:30	245.3676, 15.5876	00:18:57	Rising	60
	2013-09-03, 08:59:09	58.1361, 4.3083	12:51:41	Setting	61

Table A1
Continued

Instrument	UT ^a	Tangent point ^b	Local time ^c	Type	Group
(Obs.ID)	(HH:MM:SS)	Long, lat (°)	(HH:MM:SS)		
NuSTAR/FPM (10002001008)	2014-10-02, 03:23:18	286.5470, 13.8173	22:29:29	Rising	62
	2014-10-02, 04:24:24	97.8869, 2.3433	10:55:55	Setting	63
	2014-10-02, 05:00:08	262.2535, 13.8614	22:29:08	Rising	62
	2014-10-02, 06:01:15	73.6147, 2.3598	10:55:41	Setting	63
	2014-10-02, 06:36:58	237.9601, 13.9053	22:28:48	Rising	62
	2014-10-02, 07:38:05	49.3375, 2.3531	10:55:26	Setting	63
	2014-10-02, 08:13:49	213.6728, 13.9254	22:28:30	Rising	62
	2014-10-02, 09:14:56	25.0655, 2.3706	10:55:10	Setting	63
NuSTAR/FPM (10002001009)	2016-04-01, 07:20:28	47.9118, 13.9393	10:32:06	Rising	64
	2016-04-01, 08:21:27	219.3273, 2.3173	22:58:45	Setting	65
	2016-04-01, 08:57:09	23.6581, 13.9778	10:31:45	Rising	64
	2016-04-01, 09:58:08	195.0895, 2.3163	22:58:28	Setting	65
	2016-04-01, 10:33:50	359.4044, 14.0159	10:31:27	Rising	64
	2016-04-01, 11:34:50	170.8569, 2.3396	22:58:14	Setting	65
	2016-04-01, 12:10:32	335.1568, 14.0299	10:31:09	Rising	64
	2016-04-01, 13:11:31	146.6191, 2.3395	22:57:59	Setting	65
NuSTAR/FPM (10202001006)	2017-02-19, 19:49:00	92.6967, 14.5072	01:59:47	Setting	66
	2017-02-19, 21:25:40	68.4563, 14.4823	01:59:29	Setting	66
	2017-02-19, 23:02:20	44.2117, 14.4588	01:59:09	Setting	66
	2017-02-20, 00:39:00	19.9671, 14.4348	01:58:51	Setting	66
NuSTAR/FPM (10302001002)	2017-09-02, 07:37:03	256.2480, 4.2871	00:42:02	Rising	67
	2017-09-02, 08:38:20	69.0233, 15.4090	13:14:25	Setting	68
	2017-09-02, 09:13:43	232.0362, 4.2403	00:41:51	Rising	67
	2017-09-02, 10:15:00	44.7982, 15.4209	13:14:11	Setting	68
	2017-09-02, 10:50:23	207.8203, 4.1923	00:41:39	Rising	67
	2017-09-02, 11:51:39	20.5630, 15.4056	13:13:54	Setting	68
	2017-09-02, 12:27:03	183.6087, 4.1462	00:41:29	Rising	67
	2017-09-02, 13:28:19	356.3337, 15.4183	13:13:38	Setting	68
NuSTAR/FPM (10302001004)	2017-09-29, 18:29:01	62.0202, 14.2942	22:37:05	Rising	69
	2017-09-29, 19:30:02	233.6046, 2.3753	11:04:27	Setting	70
	2017-09-29, 20:05:40	37.7792, 14.3291	22:36:47	Rising	69
	2017-09-29, 21:06:41	209.3772, 2.3787	11:04:10	Setting	70
	2017-09-29, 21:42:20	13.5400, 14.3374	22:36:29	Rising	69
	2017-09-29, 22:43:21	185.1551, 2.4071	11:03:57	Setting	70
	2017-09-29, 23:18:59	349.2991, 14.3715	22:36:10	Rising	69
	2017-09-30, 00:20:00	160.9278, 2.4113	11:03:42	Setting	70
	2017-09-30, 00:55:38	325.0540, 14.4036	22:35:49	Rising	69
	2017-09-30, 01:56:40	136.7058, 2.4407	11:03:29	Setting	70
	2017-09-30, 02:32:17	300.8132, 14.4371	22:35:31	Rising	69
	2017-09-30, 03:33:19	112.4785, 2.4457	11:03:12	Setting	70
NuSTAR/FPM (10402001004)	2018-03-13, 00:18:24	174.8090, 9.5597	11:57:38	Rising	71
	2018-03-13, 01:20:06	348.7072, 13.2345	00:34:54	Setting	72

Table A1
Continued

Instrument (Obs.ID)	UT ^a (HH:MM:SS)	Tangent point ^b Long, lat (°)	Local time ^c (HH:MM:SS)	Type	Group
NuSTAR/FPM (10402001008)	2018-03-13, 01:55:04	150.6043, 9.4813	11:57:29	Rising	71
	2018-03-13, 02:56:45	324.4931, 13.2702	00:34:42	Setting	72
	2018-03-13, 03:31:43	126.3984, 9.4373	11:57:18	Rising	71
	2018-03-13, 04:33:25	300.2886, 13.3366	00:34:33	Setting	72
	2018-03-14, 11:44:51	2.2749, 8.2658	11:53:56	Rising	73
	2018-03-14, 12:46:29	176.0298, 14.1074	00:30:36	Setting	74
	2018-03-14, 13:21:30	338.0655, 8.2195	11:53:44	Rising	73
	2018-03-14, 14:23:08	151.8128, 14.1372	00:30:23	Setting	74
	2018-03-14, 14:58:10	313.8656, 8.1428	11:53:36	Rising	73
	2018-03-14, 15:59:47	127.5960, 14.1665	00:30:10	Setting	74
	2018-03-14, 16:34:49	289.6562, 8.0966	11:53:26	Rising	73
NuSTAR/FPM (10502001006)	2018-03-14, 17:36:27	103.3889, 14.2259	00:30:00	Setting	74
	2018-03-14, 18:11:29	265.4564, 8.0200	11:53:17	Rising	73
	2018-03-14, 19:13:06	79.1722, 14.2544	00:29:47	Setting	74
	2019-03-11, 05:34:03	100.7470, 2.6298	12:17:2	Rising	75
	2019-03-11, 06:34:41	271.1959, 11.1829	00:39:28	Setting	76
NuSTAR/FPM (10502001008)	2019-03-11, 07:10:41	76.5135, 2.6532	12:16:44	Rising	75
	2019-03-11, 08:11:19	246.9517, 11.1325	00:39:06	Setting	76
	2019-03-11, 08:47:19	52.2800, 2.6770	12:16:26	Rising	75
	2019-03-11, 09:47:57	222.7075, 11.0821	00:38:45	Setting	76
NuSTAR/FPM (10502001013)	2019-03-11, 18:27:08	266.5429, 2.7104	12:13:18	Rising	77
	2019-03-11, 19:27:45	76.8998, 10.8750	00:35:20	Setting	78
	2019-03-11, 20:03:46	242.3092, 2.7370	12:13:00	Rising	77
NuSTAR/FPM (10502001015)	2019-03-11, 21:04:23	52.6511, 10.8252	00:34:59	Setting	78
	2019-08-29, 10:10:21	217.6229, 15.3713	00:40:50	Rising	79
	2019-08-29, 11:11:40	30.3802, 4.3013	13:13:10	Setting	80
	2019-08-29, 11:46:59	193.3996, 15.3712	00:40:33	Rising	79
	2019-08-29, 12:48:18	6.1695, 4.3354	13:12:57	Setting	80
	2019-08-29, 13:23:37	169.1763, 15.3705	00:40:18	Rising	79
	2019-08-29, 14:24:56	341.9589, 4.3697	13:12:46	Setting	80
	2019-08-29, 15:00:15	144.9487, 15.3677	00:40:01	Rising	79
	2019-08-29, 16:01:35	317.7577, 4.4317	13:12:36	Setting	80
	2019-08-29, 16:36:53	120.7253, 15.3661	00:39:47	Rising	79
	2019-08-29, 17:38:13	293.5470, 4.4667	13:12:24	Setting	80
NuSTAR/FPM (10502001015)	2019-08-29, 18:13:31	96.5019, 15.3640	00:39:30	Rising	79
	2019-08-29, 19:14:51	269.3362, 4.5021	13:12:11	Setting	80
	2019-08-29, 19:50:09	72.2785, 15.3615	00:39:15	Rising	79
	2019-08-29, 20:51:30	245.1349, 4.5651	13:12:02	Setting	80
	2019-08-30, 08:43:13	238.4968, 15.3279	00:37:12	Rising	81
NuSTAR/FPM (10502001015)	2019-08-30, 09:44:37	51.4801, 4.9439	13:10:32	Setting	82
	2019-08-30, 10:19:51	214.2773, 15.3231	00:36:56	Rising	81
	2019-08-30, 11:21:15	27.2690, 4.9821	13:10:18	Setting	82

Table A1
Continued

Instrument	UT ^a	Tangent point ^b	Local time ^c	Type	Group
(Obs.ID)	(HH:MM:SS)	Long, lat (°)	(HH:MM:SS)		
NuSTAR/FPM (10602002002)	2019-08-30, 11:56:30	190.0638, 15.2882	00:36:45	Rising	81
	2019-08-30, 12:57:53	3.0620, 5.0188	13:10:06	Setting	82
	2019-08-30, 13:33:08	165.8400, 15.2806	00:36:29	Rising	81
	2019-08-30, 14:34:32	338.8603, 5.0855	13:09:57	Setting	82
	2019-08-30, 15:09:46	141.6205, 15.2742	00:36:14	Rising	81
	2019-08-30, 16:11:10	314.6490, 5.1244	13:09:44	Setting	82
	2019-08-30, 16:46:24	117.4009, 15.2674	00:36:0	Rising	81
	2019-08-30, 17:47:48	290.4419, 5.1619	13:9:33	Setting	82
	2019-08-30, 18:23:02	93.1771, 15.2584	00:35:44	Rising	81
	2019-08-30, 19:24:27	266.2401, 5.2296	13:09:24	Setting	82
NuSTAR/FPM (10602002004)	2020-02-27, 01:52:08	166.8508, 5.6676	12:59:31	Rising	83
	2020-02-27, 02:52:38	336.6918, 6.6537	01:19:23	Setting	84
	2020-02-27, 03:28:45	142.6076, 5.7239	12:59:09	Rising	83
	2020-02-27, 04:29:15	312.4440, 6.5964	01:19:00	Setting	84
	2020-02-27, 05:05:23	118.3693, 5.7626	12:58:50	Rising	83
	2020-02-27, 06:05:53	288.2054, 6.5555	01:18:42	Setting	84
NuSTAR/FPM (10602002006)	2020-02-28, 00:24:52	187.4582, 6.3583	12:54:41	Rising	85
	2020-02-28, 01:25:22	357.2962, 5.9578	01:14:32	Setting	86
	2020-02-28, 02:01:29	163.2149, 6.4171	12:54:20	Rising	85
	2020-02-28, 03:01:59	333.0528, 5.9013	01:14:11	Setting	86
	2020-02-28, 03:38:07	138.9766, 6.4582	12:54:01	Rising	85
	2020-02-28, 04:38:37	308.8104, 5.8645	01:13:50	Setting	86
NuSTAR/FPM (10602002008)	2020-08-28, 09:35:02	231.5389, 3.8916	01:01:10	Rising	87
	2020-08-28, 10:36:17	44.1504, 15.3800	13:32:53	Setting	88
	2020-08-28, 11:11:39	207.3275, 3.8718	01:00:56	Rising	87
	2020-08-28, 12:12:54	19.9219, 15.3664	13:32:35	Setting	88
	2020-08-28, 12:48:17	183.1217, 3.8242	01:00:46	Rising	87
	2020-08-28, 13:49:31	355.6977, 15.3505	13:32:17	Setting	88
NuSTAR/FPM (10702303002)	2020-08-29, 04:54:34	301.0417, 3.4484	00:58:42	Rising	89
	2020-08-29, 05:55:45	113.4503, 15.2920	13:29:32	Setting	90
	2020-08-29, 06:31:11	276.8268, 3.4309	00:58:28	Rising	89
	2020-08-29, 07:32:22	89.2221, 15.2732	13:29:15	Setting	90
	2020-08-29, 08:07:49	252.6215, 3.3880	00:58:18	Rising	89
	2020-08-29, 09:09:00	64.9998, 15.2813	13:28:59	Setting	90
NuSTAR/FPM (10702303004)	2021-02-24, 02:02:25	162.7668, 15.4134	12:53:29	Rising	91
	2021-02-24, 03:03:38	335.4311, 3.9672	01:25:21	Setting	92
	2021-02-24, 03:39:02	138.5451, 15.4127	12:53:12	Rising	91
	2021-02-24, 04:40:16	311.2310, 4.0295	01:25:10	Setting	92
	2021-02-24, 05:15:39	114.3234, 15.4115	12:52:55	Rising	91
	2021-02-24, 06:16:53	287.0255, 4.0638	01:24:59	Setting	92
NuSTAR/FPM (10702303004)	2021-02-24, 19:45:11	256.3431, 15.4164	12:50:32	Rising	93
	2021-02-24, 20:46:28	69.1889, 4.4436	01:23:12	Setting	94

Table A1
Continued

Instrument (Obs.ID)	UT ^a (HH:MM:SS)	Tangent point ^b Long, lat (°)	Local time ^c (HH:MM:SS)	Type	Group
NuSTAR/FPM (10702303006)	2021-02-24, 21:21:48	232.1256, 15.4122	12:50:17	Rising	93
	2021-02-24, 22:23:05	44.9830, 4.4811	01:22:59	Setting	94
	2021-02-24, 22:58:24	207.9022, 15.4366	12:49:59	Rising	93
	2021-02-24, 23:59:42	20.7811, 4.5173	01:22:49	Setting	94
	2021-08-28, 15:50:19	135.8574, 8.4183	00:53:44	Rising	95
	2021-08-28, 16:50:49	305.8260, 4.1961	13:14:07	Setting	96
	2021-08-28, 17:26:55	111.6184, 8.4748	00:53:22	Rising	95
	2021-08-28, 18:27:25	281.5903, 4.1548	13:13:45	Setting	96
NuSTAR/FPM (10702303008)	2021-08-28, 19:03:31	87.3795, 8.5313	00:53:02	Rising	95
	2021-08-28, 20:04:01	257.3587, 4.1121	13:13:27	Setting	96
	2021-08-29, 07:56:20	253.4673, 8.9665	00:50:12	Rising	97
	2021-08-29, 08:56:51	63.5047, 3.8224	13:10:51	Setting	98
	2021-08-29, 09:32:56	229.2247, 9.0214	00:49:49	Rising	97
	2021-08-29, 10:33:27	39.2736, 3.7825	13:10:32	Setting	98
	2021-08-29, 11:09:32	204.9864, 9.0780	00:49:27	Rising	97
	2021-08-29, 12:10:03	15.0386, 3.7447	13:10:11	Setting	98
NuSTAR/FPM (10802303002)	2022-02-24, 02:33:19	160.0056, 4.0911	13:13:19	Rising	99
	2022-02-24, 03:34:33	332.6630, 15.2855	01:45:11	Setting	100
	2022-02-24, 04:09:54	135.8067, 4.0655	13:13:06	Rising	99
	2022-02-24, 05:11:08	308.4491, 15.2763	01:44:54	Setting	100
	2022-02-24, 05:46:30	111.6091, 4.0102	13:12:56	Rising	99
Hitomi/HXI (100044010)	2022-02-24, 06:47:43	284.2311, 15.2684	01:44:38	Setting	100
	2016-03-25, 14:52:43	144.4674, 36.2736	00:30:34	Setting	101
	2016-03-25, 16:28:44	120.3037, 36.1348	00:29:56	Setting	101

^aUniversal time when the line-of-sight tangential altitude becomes 100 km. ^bLatitude and longitude of the tangent point at 100-km altitude. ^cLocal time of the tangent point at 100-km altitude.

Acknowledgments

We thank Mina Ogawa and Tadayasu Dotani for providing us with information about position uncertainties on Japanese X-ray astronomy satellites, and Ryo Iizuka for suggesting a method to correct for Hitomi satellite's positions in the housekeeping file. Craig B. Markwardt and Wataru Iwakiri gave us helpful comments on the analysis of RXTE data. Brandon Rhodes helped us use skyfield to calculate satellites' positions in various coordinates, using TLE + SGP4, T.S. Kelso pointed out bad TLE data for the ASCA satellite. We also thank Ryosuke Yasui, Hitoshi Fujiwara, and Titus Yuan for their expertized comments on the upper atmosphere. We are grateful to two referees who gave us constructive comments that improved the quality of the paper. This work was supported by the Japan Society for the Promotion of Science KAKENHI Grant 20K20935 (S.K. and M.S.T.) and 22H01267 (T.E.). This work was partly supported by Leading Initiative for Excellent Young Researchers, MEXT, Japan.

Data Availability Statement

All the data used in this paper can be found at NASA's HEASARC website, <https://heasarc.gsfc.nasa.gov/cgi-bin/W3Browse/w3browse.pl>.

References

- Aikin, A. C., Hedin, A. E., Kendig, D. J., & Drake, S. (1993). Thermospheric molecular oxygen measurements using the ultraviolet spectrometer on the Solar Maximum Mission spacecraft. *Journal of Geophysical Research*, 98(A10), 17607–17614. <https://doi.org/10.1029/93JA01468>
- Akmaev, R. A., Fomichev, V. I., & Zhu, X. (2006). Impact of middle-atmospheric composition changes on greenhouse cooling in the upper atmosphere. *Journal of Atmospheric and Solar-Terrestrial Physics*, 68(17), 1879–1889. <https://doi.org/10.1016/j.jastp.2006.03.008>
- Arnaud, K. A. (1996). XSPEC: The first ten years. In G. H. Jacoby, & J. Barnes (Eds.), *Astronomical data analysis software and systems v* (Vol. 101, p. 17).
- Bailey, S. M., Thuraijajah, B., Hervig, M. E., Siskind, D. E., Russell, J. M., & Gordley, L. L. (2021). Trends in the polar summer mesosphere temperature and pressure altitude from satellite observations. *Journal of Atmospheric and Solar-Terrestrial Physics*, 220, 105650. <https://doi.org/10.1016/j.jastp.2021.105650>
- Beig, G. (2011). Long-term trends in the temperature of the mesosphere/lower thermosphere region: 2. Solar response. *Journal of Geophysical Research*, 116, A00H12. <https://doi.org/10.1029/2011JA016766>
- Bernhard, G., & Stierle, S. (2020). Trends of UV radiation in Antarctica. *Atmosphere*, 11(8), 795. <https://doi.org/10.3390/atmos11080795>
- Bhalerao, V. (2012). *Neutron stars and NuSTAR (Unpublished doctoral dissertation)*. California Institute of Technology.

- Bowman, B. R., Tobiska, W. K., Marcos, F. A., Huang, C. Y., Lin, C. S., & Burke, W. J. (2008). A new empirical thermospheric density model JB2008 using new solar and geomagnetic indices. Paper AIAA 2008–6438 presented at AIAA/AAS Astrodynamics Specialist Conference and Exhibit, Honolulu, Hawaii: Am. Inst. of Aeronaut. and Astronaut.
- Bremer, J. (2008). Long-term trends in the ionospheric E and F1 regions. *Annales Geophysicae*, 26(5), 1189–1197. <https://doi.org/10.5194/angeo-26-1189-2008>
- Bremer, J., & Peters, D. (2008). Influence of stratospheric ozone changes on long-term trends in the meso- and lower thermosphere. *Journal of Atmospheric and Solar-Terrestrial Physics*, 70(11–12), 1473–1481. <https://doi.org/10.1016/j.jastp.2008.03.024>
- Clemesha, B. R., Batista, P. P., & Simonich, D. M. (1997). Long-term and solar cycle changes in the atmospheric sodium layer. *Journal of Atmospheric and Solar-Terrestrial Physics*, 59(13), 1673–1678. [https://doi.org/10.1016/S1364-6826\(96\)00166-6](https://doi.org/10.1016/S1364-6826(96)00166-6)
- Cnossen, I. (2020). Analysis and attribution of climate change in the upper atmosphere from 1950 to 2015 simulated by WACCM-X. *Journal of Geophysical Research: Space Physics*, 125, e2020JA028623. <https://doi.org/10.1029/2020JA028623>
- Cnossen, I., Liu, H., & Lu, H. (2016). The whole atmosphere response to changes in the Earth's magnetic field from 1900 to 2000: An example of “top-down” vertical coupling. *Journal of Geophysical Research: Atmospheres*, 121, 7781–7800. <https://doi.org/10.1002/2016JD024890>
- Danilov, A. D., & Konstantinova, A. V. (2020). Long-term variations in the parameters of the middle and upper atmosphere and ionosphere (Review). *Geomagnetism and Aeronomy*, 60(4), 397–420. <https://doi.org/10.1134/S0016793220040040>
- Determan, J. R., Budzien, S. A., Kowalski, M. P., Lovellette, M. N., Ray, P. S., Wolff, M. T., et al. (2007). Measuring atmospheric density with X-ray occultation sounding. *Journal of Geophysical Research*, 112, A06323. <https://doi.org/10.1029/2006JA012014>
- Emmert, J. T. (2015). Altitude and solar activity dependence of 1967–2005 thermospheric density trends derived from orbital drag. *Journal of Geophysical Research: Space Physics*, 120, 2940–2950. <https://doi.org/10.1002/2015JA021047>
- Emmert, J. T., Drob, D. P., Picone, J. M., Siskind, D. E., Jones, M., Mlynczak, M. G., et al. (2021). NRLMSIS 2.0: A whole atmosphere empirical model of temperature and neutral species densities. *Earth and Space Science*, 8, e2020EA001321. <https://doi.org/10.1029/2020EA001321>
- Emmert, J. T., Picone, J. M., & Meier, R. R. (2008). Thermospheric global average density trends, 1967–2007, derived from orbits of 5000 near-Earth objects. *Geophysical Research Letters*, 35, L05101. <https://doi.org/10.1029/2007GL032809>
- Emmert, J. T., Stevens, M. H., Bernath, P. F., Drob, D. P., & Boone, C. D. (2012). Observations of increasing carbon dioxide concentration in Earth's thermosphere. *Nature Geoscience*, 5(12), 868–871. <https://doi.org/10.1038/ngeo1626>
- Fiedler, J., Baumgarten, G., Berger, U., & Lübken, F.-J. (2017). Long-term variations of noctilucent clouds at ALOMAR. *Journal of Atmospheric and Solar-Terrestrial Physics*, 162, 79–89. <https://doi.org/10.1016/j.jastp.2016.08.006>
- Friedrich, M., Pock, C., & Torkar, K. (2017). Long-term trends in the D- and E-region based on rocket-borne measurements. *Journal of Atmospheric and Solar-Terrestrial Physics*, 163, 78–84. <https://doi.org/10.1016/j.jastp.2017.04.009>
- García, R. R., López-Puertas, M., Funke, B., Kinnison, D. E., Marsh, D. R., & Qian, L. (2016). On the secular trend of CO_x and CO₂ in the lower thermosphere. *Journal of Geophysical Research: Atmospheres*, 121, 3634–3644. <https://doi.org/10.1002/2015JD024553>
- Goessling, H. F., & Bathiany, S. (2016). Why CO₂ cools the middle atmosphere—A consolidating model perspective. *Earth System Dynamics*, 7(3), 697–715. <https://doi.org/10.5194/esd-7-697-2016>
- Hall, C. M., Holmen, S. E., Meek, C. E., Manson, A. H., & Nozawa, S. (2016). Change in turbopause altitude at 52 and 70°N. *Atmospheric Chemistry and Physics*, 16(4), 2299–2308. <https://doi.org/10.5194/acp-16-2299-2016>
- Harrison, F. A., Craig, W. W., Christensen, F. E., Hailey, C. J., Zhang, W. W., Boggs, S. E., et al. (2013). The Nuclear Spectroscopic Telescope Array (NuSTAR) high-energy X-ray mission. *The Astrophysical Journal*, 770(2), 103. <https://doi.org/10.1088/0004-637X/770/2/103>
- Hubbell, J. H., Gimm, H. A., & Øverbø, I. (1980). Pair, triplet, and total atomic cross sections (and mass attenuation coefficients) for 1 MeV–100 GeV photons in elements Z=1 to 100. *Journal of Physical and Chemical Reference Data*, 9(4), 1023–1148. <https://doi.org/10.1063/1.555629>
- Jahoda, K., Markwardt, C. B., Radeva, Y., Rots, A. H., Stark, M. J., Swank, J. H., et al. (2006). Calibration of the Rossi X-ray timing explorer proportional counter array. *The Astrophysical Journal-Supplement Series*, 163(2), 401–423. <https://doi.org/10.1086/500659>
- Jahoda, K., Swank, J. H., Giles, A. B., Stark, M. J., Strohmayer, T., Zhang, W., & Morgan, E. H. (1996). In-orbit performance and calibration of the Rossi X-ray Timing Explorer (RXTE) Proportional Counter Array (PCA). In O. H. Siegmund, & M. A. Gummin (Eds.), *EUV, X-ray, and gamma-ray instrumentation for astronomy VII* (Vol. 2808, pp. 59–70). <https://doi.org/10.1117/12.256034>
- Katsuda, S., Fujiwara, H., Ishisaki, Y., Yoshitomo, M., Mori, K., Motizuki, Y., et al. (2021). New measurement of the vertical atmospheric density profile from occultations of the Crab Nebula with X ray astronomy satellites Suzaku and Hitomi. *Journal of Geophysical Research: Space Physics*, 126, e2020JA028886. <https://doi.org/10.1029/2020JA028886>
- Koyama, K., Tsunemi, H., Dotani, T., Bautz, M. W., Hayashida, K., Tsuru, T. G., et al. (2007). X-ray imaging spectrometer (XIS) on board Suzaku. *Publications of the Astronomical Society of Japan*, 59, 23–33. <https://doi.org/10.1093/pasj/59.sp1.S23>
- Laštovička, J. (2015). Comment on “Long-term trends in thermospheric neutral temperatures and density above Millstone Hill” by W. L. Oliver et al. *Journal of Geophysical Research: Space Physics*, 120, 2347–2349. <https://doi.org/10.1002/2014JA020864>
- Laštovička, J. (2017). A review of recent progress in trends in the upper atmosphere. *Journal of Atmospheric and Solar-Terrestrial Physics*, 163, 2–13. <https://doi.org/10.1016/j.jastp.2017.03.009>
- Laštovička, J., & Jelínek, Š. (2019). Problems in calculating long-term trends in the upper atmosphere. *Journal of Atmospheric and Solar-Terrestrial Physics*, 189, 80–86. <https://doi.org/10.1016/j.jastp.2019.04.011>
- López-Puertas, M., Funke, B., Jurado-Navarro, Á. A., García-Comas, M., Gardini, A., Boone, C. D., et al. (2017). Validation of the MIPAS CO₂ volume mixing ratio in the mesosphere and lower thermosphere and comparison with WACCM simulations. *Journal of Geophysical Research: Atmospheres*, 122, 8345–8366. <https://doi.org/10.1002/2017JD026805>
- Lübken, F.-J., Baumgarten, G., & Berger, U. (2021). Long term trends of mesospheric ice layers: A model study. *Journal of Atmospheric and Solar-Terrestrial Physics*, 214, 105378. <https://doi.org/10.1016/j.jastp.2020.105378>
- Lübken, F. J., Berger, U., & Baumgarten, G. (2013). Temperature trends in the midlatitude summer mesosphere. *Journal of Geophysical Research: Atmospheres*, 118, 13347–13360. <https://doi.org/10.1002/2013JD020576>
- Madsen, K. K., Reynolds, S., Harrison, F., An, H., Boggs, S., Christensen, F. E., et al. (2015). Broadband X-ray imaging and spectroscopy of the Crab Nebula and Pulsar with NuSTAR. *The Astrophysical Journal*, 801(1), 66. <https://doi.org/10.1088/0004-637X/801/1/66>
- Maillard Barras, E., Haefele, A., Nguyen, L., Tummon, F., Ball, W. T., Rozanov, E. V., et al. (2020). Study of the dependence of long-term stratospheric ozone trends on local solar time. *Atmospheric Chemistry and Physics*, 20(14), 8453–8471. <https://doi.org/10.5194/acp-20-8453-2020>
- Makishima, K., Tashiro, M., Ebisawa, K., Ezawa, H., Fukazawa, Y., Gunji, S., et al. (1996). In-orbit performance of the gas imaging spectrometer onboard ASCA. *Publications of the Astronomical Society of Japan*, 48, 171–189. <https://doi.org/10.1093/pasj/48.2.171>
- Manabe, S., & Wetherald, R. T. (1967). Thermal equilibrium of the atmosphere with a given distribution of relative humidity. *Journal of the Atmospheric Sciences*, 24(3), 241–259. [https://doi.org/10.1175/1520-0469\(1967\)024<241:TEOTAW>2.0.CO;2](https://doi.org/10.1175/1520-0469(1967)024<241:TEOTAW>2.0.CO;2)
- Matsuno, T. (1971). A dynamical model of the stratospheric sudden warming. *Journal of the Atmospheric Sciences*, 28(8), 1479–1494. [https://doi.org/10.1175/1520-0469\(1971\)028<1479:ADMOTS>2.0.CO;2](https://doi.org/10.1175/1520-0469(1971)028<1479:ADMOTS>2.0.CO;2)

- Meier, R. R., Picone, J. M., Drob, D., Bishop, J., Emmert, J. T., Lean, J. L., et al. (2015). Remote Sensing of Earth's Limb by TIMED/GUVI: Retrieval of thermospheric composition and temperature. *Earth and Space Science*, 2, 1–37. <https://doi.org/10.1002/2014EA000035>
- Mitsuda, K., Bautz, M., Inoue, H., Kelley, R. L., Koyama, K., Kunieda, H., et al. (2007). The X-ray observatory Suzaku. *Publications of the Astronomical Society of Japan*, 59, S1–S7. <https://doi.org/10.1093/pasj/59.sp1.S1>
- Nakazawa, K., Sato, G., Kokubun, M., Enoto, T., Fukazawa, Y., Hagino, K., et al. (2018). Hard x-ray imager onboard Hitomi (ASTRO-H). *Journal of Astronomical Telescopes, Instruments, and Systems*, 4(2), 021410. <https://doi.org/10.1117/1.JATIS.4.2.021410>
- Norton, R. B., & Warnock, J. M. (1968). Seasonal variation of molecular oxygen near 100 kilometers. *Journal of Geophysical Research*, 73(17), 5798–5800. <https://doi.org/10.1029/JA073i017p05798>
- Ohashi, T., Ebisawa, K., Fukazawa, Y., Hiyoshi, K., Horii, M., Ikebe, Y., et al. (1996). The gas imaging spectrometer on board ASCA. *Publications of the Astronomical Society of Japan*, 48, 157–170. <https://doi.org/10.1093/pasj/48.2.157>
- Pedregosa, F., Varoquaux, G., Gramfort, A., Michel, V., Thirion, B., Grisel, O., et al. (2011). Scikit-learn: Machine learning in python. *Journal of Machine Learning Research*, 12(85), 2825–2830.
- Perrone, L., & Mikhailov, A. V. (2019). Long-term variations of June column atomic oxygen abundance in the upper atmosphere inferred from ionospheric observations. *Journal of Geophysical Research: Space Physics*, 124, 6305–6312. <https://doi.org/10.1029/2019JA026818>
- Peters, D. H. W., & Entzian, G. (2015). Long-term variability of 50 years of standard phase-height measurement at Kühlungsborn, Mecklenburg, Germany. *Advances in Space Research*, 55(7), 1764–1774. <https://doi.org/10.1016/j.asr.2015.01.021>
- Peters, D. H. W., Entzian, G., & Keckhut, P. (2017). Mesospheric temperature trends derived from standard phase-height measurements. *Journal of Atmospheric and Solar-Terrestrial Physics*, 163, 23–30. <https://doi.org/10.1016/j.jastp.2017.04.007>
- Pokhunkov, A. A., Rybin, V. V., & Tulinov, G. F. (2009). Quantitative characteristics of long-term changes in parameters of the upper atmosphere of the Earth over the 1966–1992 period. *Cosmic Research*, 47(6), 480–490. <https://doi.org/10.1134/S0010952509060045>
- Qian, L., Marsh, D., Merkel, A., Solomon, S. C., & Roble, R. G. (2013). Effect of trends of middle atmosphere gases on the mesosphere and thermosphere. *Journal of Geophysical Research: Space Physics*, 118, 3846–3855. <https://doi.org/10.1002/jgra.50354>
- Rezac, L., Yue, J., Yongxiao, J., Russell, J. M., Garcia, R., López-Puertas, M., & Mlynarczyk, M. G. (2018). On long-term SABER CO2 trends and effects due to nonuniform space and time sampling. *Journal of Geophysical Research: Space Physics*, 123, 7958–7967. <https://doi.org/10.1029/2018JA025892>
- Roble, R. G., & Dickinson, R. E. (1989). How will changes in carbon dioxide and methane modify the mean structure of the mesosphere and thermosphere? *Geophysical Research Letters*, 16(12), 1441–1444. <https://doi.org/10.1029/GL016i012p01441>
- Russell, J. M., Mlynarczyk, M. G., Gordley, L. L., Tansock, J. J., & Esplin, R. W. (1999). Overview of the SABER experiment and preliminary calibration results. In A. M. Larar (Ed.), *Optical spectroscopic techniques and instrumentation for atmospheric and space research iii* (Vol. 3756, pp. 277–288). <https://doi.org/10.1117/12.366382>
- Sato, K., Yasui, R., & Miyoshi, Y. (2018). The momentum budget in the stratosphere, mesosphere, and lower thermosphere. Part I: Contributions of different wave types and in situ generation of Rossby waves. *Journal of the Atmospheric Sciences*, 75(10), 3613–3633. <https://doi.org/10.1175/JAS-D-17-0336.1>
- Solomon, S. C., Liu, H.-L., Marsh, D. R., McInerney, J. M., Qian, L., & Vitt, F. M. (2019). Whole atmosphere climate change: Dependence on solar activity. *Journal of Geophysical Research: Space Physics*, 124, 3799–3809. <https://doi.org/10.1029/2019JA026678>
- Solomon, S. C., Qian, L., & Roble, R. G. (2015). New 3-D simulations of climate change in the thermosphere. *Journal of Geophysical Research: Space Physics*, 120, 2183–2193. <https://doi.org/10.1002/2014JA020886>
- Stevens, M. H., Randall, C. E., Carstens, J. N., Siskind, D. E., McCormack, J. P., Kuhl, D. D., & Dhadly, M. S. (2022). Northern mid-latitude mesospheric cloud frequencies observed by AIM/CIPS: Interannual variability driven by space traffic. *Earth and Space Science*, 9, e2022EA002217. <https://doi.org/10.1029/2022EA002217>
- Stober, G., Matthias, V., Brown, P., & Chau, J. L. (2014). Neutral density variation from specular meteor echo observations spanning one solar cycle. *Geophysical Research Letters*, 41, 6919–6925. <https://doi.org/10.1002/2014GL061273>
- Strelnikov, B., Rapp, M., & Lübken, F. (2013). In-situ density measurements in the mesosphere/lower thermosphere region with the TOTAL and CONE instruments. In *An introduction to space instrumentation* (pp. 1–11). <https://doi.org/10.5047/aisi.001>
- Takahashi, T., Abe, K., Endo, M., Endo, Y., Ezoe, Y., Fukazawa, Y., et al. (2007). Hard X-ray detector (HXD) on board Suzaku. *Publications of the Astronomical Society of Japan*, 59, 35–51. <https://doi.org/10.1093/pasj/59.sp1.S35>
- Takahashi, T., Kokubun, M., Mitsuda, K., Kelley, R. L., Ohashi, T., Aharonian, F., et al. (2018). Hitomi (ASTRO-H) X-ray astronomy satellite. *Journal of Astronomical Telescopes, Instruments, and Systems*, 4(2), 021402. <https://doi.org/10.1117/1.JATIS.4.2.021402>
- Tanaka, Y., Inoue, H., & Holt, S. S. (1994). The X-ray astronomy satellite ASCA. *Publications of the Astronomical Society of Japan*, 46, L37–L41.
- Tomikawa, Y., Sato, K., Watanabe, S., Kawatani, Y., Miyazaki, K., & Takahashi, M. (2012). Growth of planetary waves and the formation of an elevated stratopause after a major stratospheric sudden warming in a T213L256 GCM. *Journal of Geophysical Research*, 117, D16101. <https://doi.org/10.1029/2011JD017243>
- Verner, D. A., Ferland, G. J., Korista, K. T., & Yakovlev, D. G. (1996). Atomic data for Astrophysics. II. New analytic FITS for photoionization cross sections of atoms and ions. *The Astrophysical Journal*, 465, 487. <https://doi.org/10.1086/177435>
- Wang, R., Liu, J., & Zhang, Q. M. (2009). Propagation errors analysis of TLE data. *Advances in Space Research*, 43(7), 1065–1069. <https://doi.org/10.1016/j.asr.2008.11.017>
- Wilhelm, S., Stober, G., & Brown, P. (2019). Climatologies and long-term changes in mesospheric wind and wave measurements based on radar observations at high and mid latitudes. *Annales Geophysicae*, 37(5), 851–875. <https://doi.org/10.5194/angeo-37-851-2019>
- Wilms, J., Allen, A., & McCray, R. (2000). On the absorption of X-rays in the interstellar medium. *The Astrophysical Journal*, 542(2), 914–924. <https://doi.org/10.1086/317016>
- Wilson-Hodge, C. A., Cherry, M. L., Case, G. L., Baumgartner, W. H., Beklen, E., Narayana Bhat, P., et al. (2011). When a standard candle flickers. *The Astrophysical Journal Letters*, 727(2), L40. <https://doi.org/10.1088/2041-8205/727/2/L40>
- Wood, K. S., Ray, P. S., Wolff, M. T., Gendreau, K., Arzoumanian, Z., Mitchell, J. W., & Winternitz, L. M. B. (2020). Satellite navigation using X-ray pulsars and horizon crossings of X-ray stars. *Advances in the Astronautical Sciences AAS Guidance, Navigation, and Control 2020*, 20, 124.
- Xu, X.-L., & Xiong, Y.-Q. (2018). Orbit error characteristic and distribution of TLE using CHAMP orbit data. *Astrophysics and Space Science*, 363(2), 31. <https://doi.org/10.1007/s10509-018-3251-z>
- Yasui, R., Sato, K., & Miyoshi, Y. (2018). The momentum budget in the stratosphere, mesosphere, and lower thermosphere. Part II: The in situ generation of gravity waves. *Journal of the Atmospheric Sciences*, 75(10), 3635–3651. <https://doi.org/10.1175/JAS-D-17-0337.1>
- Yu, D., Li, H., Li, B., Ge, M., Tuo, Y., Li, X., et al. (2022a). Measurement of the vertical atmospheric density profile from the X-ray Earth occultation of the Crab Nebula with Insight-HXMT. arXiv:2204.09674.
- Yu, D., Li, H., Li, B., Ge, M., Tuo, Y., Li, X., et al. (2022b). New method for Earth neutral atmospheric density retrieval based on energy spectrum fitting during occultation with LE/Insight-HXMT. *Advances in Space Research*, 69(9), 3426–3434. <https://doi.org/10.1016/j.asr.2022.02.030>

- Yuan, T., Solomon, S. C., She, C. Y., Krueger, D. A., & Liu, H. L. (2019). The long-term trends of nocturnal mesopause temperature and altitude revealed by Na lidar observations between 1990 and 2018 at midlatitude. *Journal of Geophysical Research*, *124*, 5970–5980. <https://doi.org/10.1029/2018JD029828>
- Yue, J., Russell, J., Gan, Q., Wang, T., Rong, P., Garcia, R., & Mlynczak, M. (2019). Increasing water vapor in the stratosphere and mesosphere after 2002. *Geophysical Research Letters*, *46*, 13452–13460. <https://doi.org/10.1029/2019GL084973>
- Zhang, S.-R., Holt, J. M., Erickson, P. J., Goncharenko, L. P., Nicolls, M. J., McCreedy, M., & Kelly, J. (2016). Ionospheric ion temperature climate and upper atmospheric long-term cooling. *Journal of Geophysical Research: Space Physics*, *121*, 8951–8968. <https://doi.org/10.1002/2016JA022971>